SAPIENZA
UNIVERSITÀ DI ROMA

Facoltà di Scienze Matematiche Fisiche e Naturali

Corso di Laurea in Fisica

Tesi di Laurea Specialistica

Studio degli eventi J/Ψ in due elettroni con i primi dati di CMS

Candidato

Shervin Nourbakhsh

Matricola

1106418

Relatore

Dott. Riccardo Paramatti

Relatore interno

Prof. Egidio Longo

Anno Accademico 2009/2010

Contents

Introduction

In April 2010, the Large Hadron Collider (LHC) started colliding proton beams at the energy of 7 TeV in the center of mass. Since then, the four experiments at the LHC experienced the continuous growing of the provided peak luminosity from 10^{27} up to $10^{31}\ \mathrm{cm}^{-2}\,\mathrm{s}^{-1}$ and above.

The Compact Muon Solenoid (CMS) experiment took advantage from the low luminosity regime in order to test the detector performances using particles produced with a low transverse momentum ($p_T < 10$ GeV). At higher luminosities, in fact, the rate of soft interactions (minimum bias events) excesses the data recording possibilities.

In this work we will present the selection of $J/\Psi \to e^+e^-$ events with the first data collected by the CMS experiment.

J/Ψ decaying into electrons can be used in order to check the absolute scale of the electromagnetic calorimeter, the selection efficiency of low p_T electrons, the electron-related distributions agreement between data and Monte Carlo (MC) simulations. This is particularly useful in the Higgs boson search in the 4 lepton decay channel $H \to ZZ^* \to 4\ell$.

The J/Ψ study at hadron colliders has also a theoretical interest as a check of different QCD production models, though the statistics available up to now is still limited for this kind of study.

The Standard Model (SM) of particle physics and the LHC physics will be briefly described in the first chapter giving the main characteristics of the J/Ψ particle. Theoretical and experimental interest are also introduced in Chapter 1.

We will provide the overview of the CMS experiment in Chapter 2, describing with more details the CMS subdetectors involved in the electron reconstruction and stressing the detector characteristics required for this analysis.

Chapter 3 is entirely dedicated to the electron reconstruction algorithms used in CMS, pointing out the difficulties in reconstructing low p_T electrons like the ones of the $J/\Psi \rightarrow e^+e^-$ decay. In fact, the reconstruction of low p_T electrons it's a challenging task since the detector was designed in order to have the best performances for electrons with a transverse momentum greater than 25 GeV (like the ones produced by the Z boson decay). Nevertheless, the reconstruction of this kind of electrons could be an important task for the Higgs hunting as explained in Sec 5.

The J/Ψ event selection developed in this analysis will be described in Chapter 4 where we will illustrate not only the strategy and techniques used to select a high purity J/Ψ sample, but also the signal yield extraction.

Chapter 5 is devoted to the efficiency studies on the electron reconstruction and selection, providing a first low p_T electron study using the first J/Ψ events. Furthermore, we will use the selected J/Ψ sample to check the electromagnetic calorimeter (ECAL) absolute scale. The single electron efficiency estimation combined with the trigger efficiency is used in a preliminarily estimation of the prompt J/Ψ cross-section.

We will then conclude summarizing the analysis results.

Chapter 1

Standard Model and LHC physics

1.1 Standard Model of particle physics

The Standard Model (SM) is one of the best verified theory of the last century. It describes with extraordinary precision the Nature at the smallest dimension experimentally accessible up to now.

It is a mathematical model describing elementary particles in the context of the Quantum Field Theory. In such a representation particles are the quanta of the fields.

Ordinary matter is made of six spin $\frac{1}{2}$ particles called leptons and six spin $\frac{1}{2}$ particles called quarks, each repeated in three "colours". They are classified in three generations and grouped in doublets.

In the SM, quarks and leptons interact with each other via three of the four fundamental forces of Nature: the strong force, the electromagnetic and the weak one. The SM does not include gravitation. The force mediators are called bosons (because the obey to the Bose-Einstein statistics), quarks and leptons are called fermions (because the obey to the Fermi-Dirac statistics).

The SM elementary particles are shown in Fig. 1.1 and their interactions are schematically shown in Fig. 1.1(b)

The motion and interaction of particles are derived from the Lagrangian of the model using the Minimal Action Principle.

The Standard Model Lagrangian is required to be invariant to the following gauge

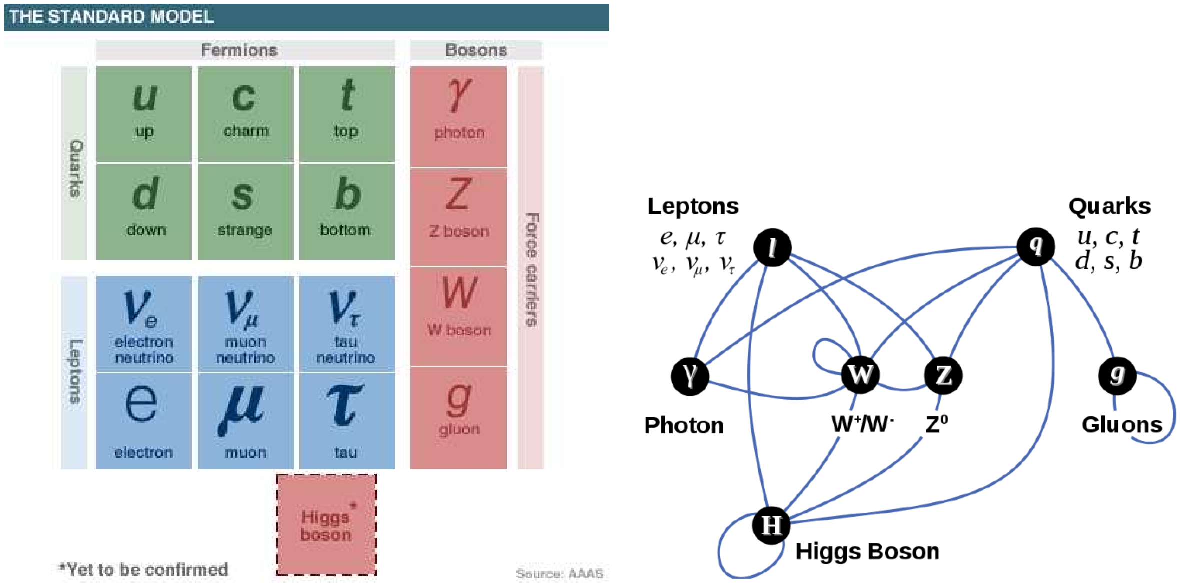

Figure 1.1: *Fig. a) shows the Standard Model elementary particles divided into ordinary matter particles called fermions (left side) and force carriers called bosons (right side). Fermions are divided into quarks (subjected to the strong force) and leptons (neutral for the strong force). Quarks and leptons are grouped in three generation of doublets. The particles masses are given by the interaction with the Higgs boson shown in the bottom. Fig. b) illustrated schematically the particle interactions,*

transformation symmetry groups:

$$SU(3)_c \times SU(2)_L \times U(1)_Y \tag{1.1}$$

The $SU(2)_L \times U(1)_Y$ invariance group represent the theoretical unification of the electromagnetic and the weak forces in the electroweak interaction[1]. The Glashow[2], Weinber[3] and Salam[4] theory derives from this symmetry group the existence and behaviour of the electroweak boson mediators (the Z^0 and $W^{\pm}$ bosons) and the electromagnetic carrier, the photon (γ).

The spontaneous symmetry breaking mechanism [5, 6] provides the way to give masses to particles preserving the gauge invariance of the Lagrangian. This is done introducing a scalar field in the theory, the Higgs field, whose quantum is the still unobserved Higgs boson.

The strong force carriers are derived by the $SU(3)_c$ term. The quark model was proposed by Gell-Mann[7] in 1964. The idea of the "colour" quantum number was introduced by Han and Nambu[8] in 1965 to avoid the apparent paradox that the quark model seemed to require a violation of the Pauli exclusion principle in order to describe the hadron spectroscopy. The Quantum Chromo-Dynamics (QCD), the strong interaction sector of the SM, was then quantized as a gauge theory with $SU(3)_c$ symmetry in 1973 by Fritzsch[9], Gross and Wilczec[10], Weinberg[11].

Due to the very high magnitude of the strong force compared to the others, we cannot find free quarks even at very high energies. Thus, the production of quarks in the collisions is revealed as jets of particles originated by the hadronization process.

A useful concept is the QCD scale Λ_{QCD}. At energies $E > \Lambda_{QCD} \simeq 150$ MeV the strong coupling constant α_s becames less than 1 and a perturbative approach to the QCD is possible.

The J/Ψ particle

In analogy to positronium (the electron-positron bound state), the heavy ($m \gg \Lambda_{\mathrm{QCD}}$) quark - antiquark bound states were named quarkonia. They are classified using the spectroscopic notation. The bound states of charm quark (c) and its anti-particle ($\bar{c}$) are known as charmonium states and they differ by orbital angular momentum (L), total spin (S), total angular momentum (J) and by mass (because of the different bounding energy). In Fig. 1.2 the charmonium system and the decay modes are shown.

The J/Ψ particle was discovered as a narrow resonance with a mass $m \sim 3.1$ GeV in the November of 1974 by two groups indipendently. The first headed by Ting in $p + Be \rightarrow e^+e^- + X$ [12] at Brookheaven and the second headed by Richter at the e^+e^- storage ring SPEAR at SLAC [13]. The J/Ψ is characterized by angular momentum $L = 1$, parity $P = -1$ and charge conjugation $C = -1$. It is an hadronic resonance represented by a Breit-Wigner distribution centered at the nominal mass [14] $m_{J/\Psi} = 3096.916 \pm 0.011$ MeV with an intrinsic width of $\Gamma = 92.9 \pm 2.8$ keV. The distribution width is inversely proportional to the particle lifetime (τ): $\Gamma = \frac{\hbar c}{\tau}$. The narrow width (and consequently the long lifetime) of the J/Ψ is due to impossibility of the particle to decay in a charmed meson pair because of their larger mass. The radiative decay mode

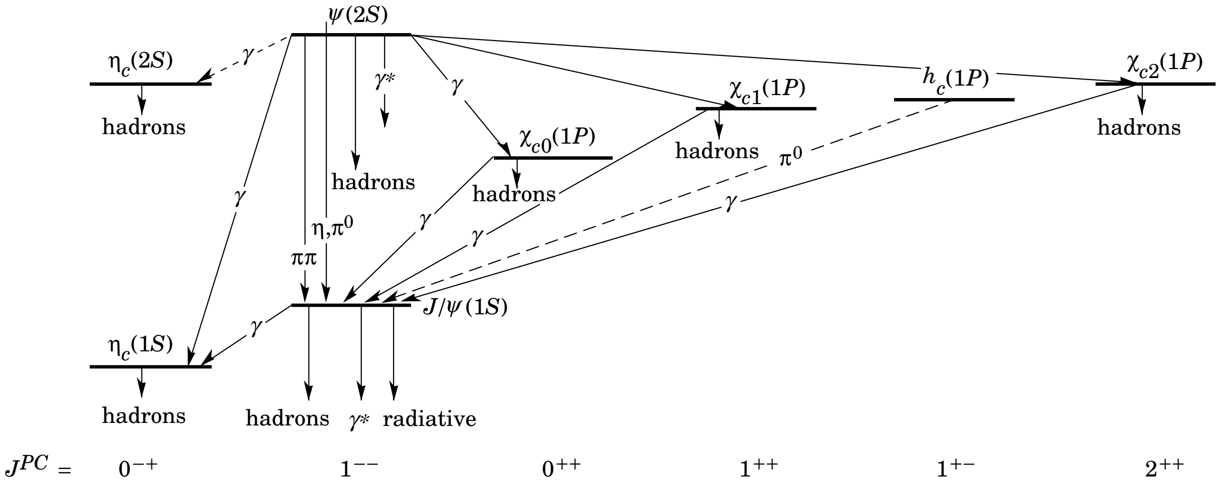

Figure 1.2: *Schematic representation of the charmonium system, showing the different $c\bar{c}$ states related to their quantum numbers and masses. The decay modes are indicated by arrows.*

into the lighter $c\bar{c}$ pair (η_c) is suppressed. The probability of decaying into a particular channel is called branching ratio (BR). The J/Ψ decay modes are:

decay channel	BR[%]
hadrons	87.7 ± 0.5
electrons	5.94 ± 0.06
muons	5.93 ± 0.06

1.2 LHC physics

The main target of particle physics for the years to come will be the comprehension of the electroweak simmetry breaking mechanism and the search for possible new physics. These are the reasons that led the particle physics community to design and build a new and more powerful accelator, the Large Hadron Collider (LHC); in this section the physics requirements and feasibility will be reviewed.

In a circular collider of radius R, the energy loss per turn due to synchrotron radiation is proportional to $\frac{1}{R} \cdot \left(\frac{E}{M}\right)^4$, where E and M are respectively the energy and mass of the particles accelerated; it then follows that a circular electron collider would need enormous dimensions to reach energies of the order of 500 GeV per beam, therefore the natural choice for a collider with current technologies is to use beams of protons, which are almost 2000 times heavier than electrons. In a proton-proton collider the interactions involve the proton constituents (quarks, anti-quarks and gluons), which carry only a fraction of the proton momentum. A drawback is that the centre-of-mass energy and the rest frame for the hard scattering are unknown, but an advantage is that a wider range of energies can be explored with respect to with fixed-energy beams.

The event rate R_i of a physics channel i occurring with cross section σ_i can be defined as the number of events per unit of time:

$$\frac{dN_i}{dt} = R_i = \sigma_i \mathcal{L} \tag{1.2}$$

and it is proportional to cross section σ_i via the constant $\mathcal{L}$, luminosity, which depends only on the machine parameters. Assuming a small crossing angle between the beams and gaussian-shaped beam bunches, the luminosity $\mathcal{L}$ can be expressed as

$$\mathcal{L} = f \frac{n_b N_1 N_2}{4\pi \sigma_x \sigma_y} \tag{1.3}$$

where f is the revolution frequency of the n_b bunches, N_1 and N_2 number of protons in the two colliding bunches, σ_x and σ_y the beam profiles in horizontal (bend) and vertical directions at the interaction point.

In the Fig. 1.3 cross-sections for different processes are given as a function of the centre of mass energy in pp collisions; in particular it can be noted how the inclusive Higgs production cross-section steeply increases with the centre of mass energy while the background, the total inelastic pp cross-section, remains approximatively constant over a wide range of energies. Therefore, it can be argued that, to raise the Higgs statistics, the highest possible centre of mass energy should be used (see Fig.1.3).

The other important characteristic to maximize the rate for a particular process is the luminosity; this has the drawback, however, that the total event rate can become so high that several interactions overlap in the same bunch crossing (pile up). The LHC characteristics will be described in the following chapter.

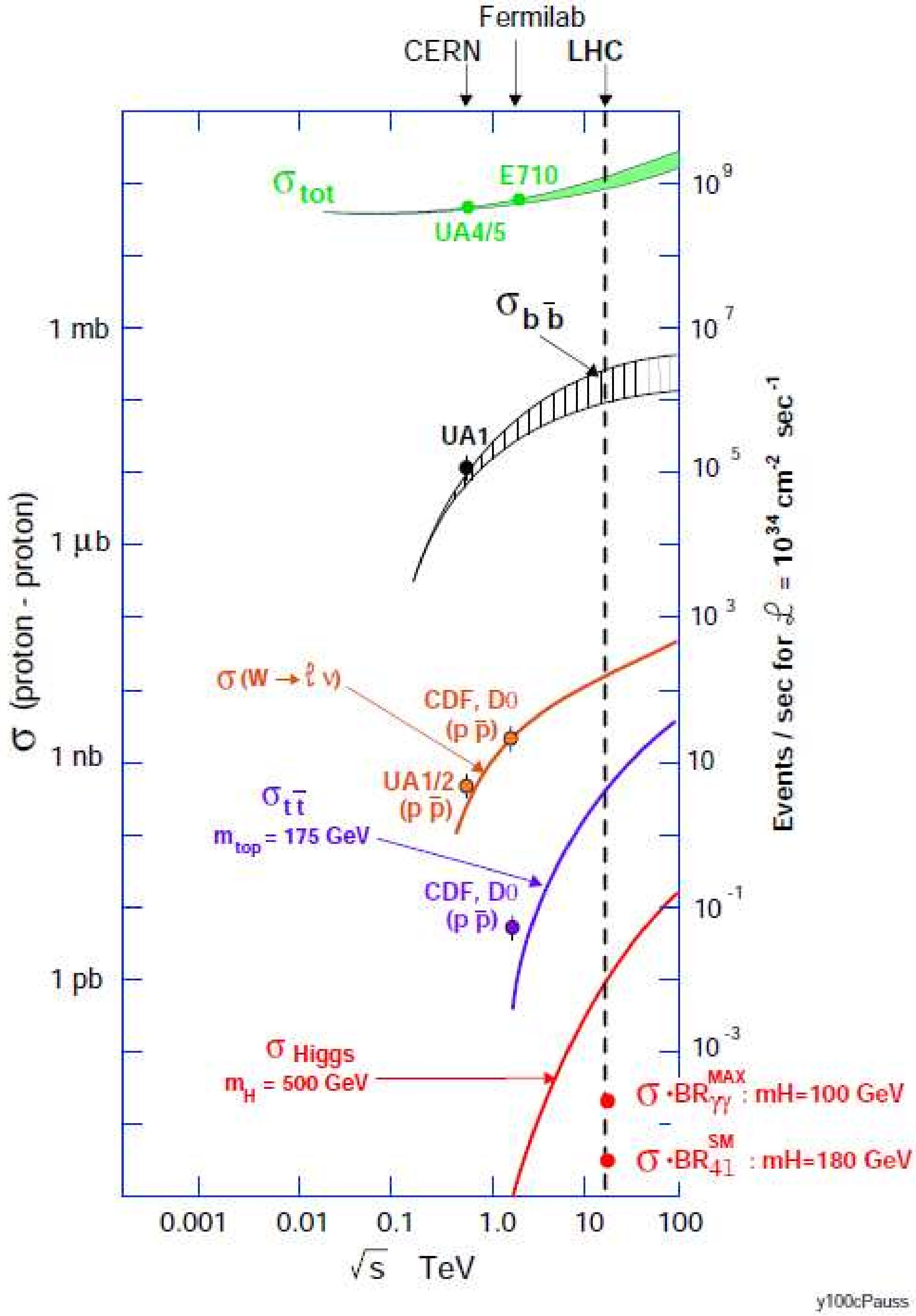

Figure 1.3: *Cross section of different processes as a function of the center of mass energy $\sqrt{s}$ in proton-proton collision. On the right vertical axis are reported the corresponding event rate given the LHC design luminosity.*

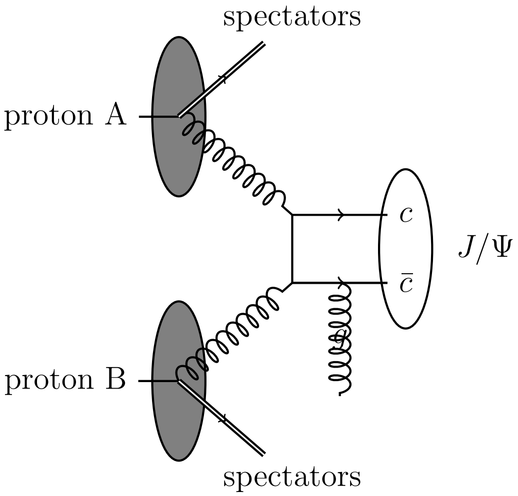

Figure 1.4: *Feynamn diagram of prompt direct J/Ψ production by gluon-gluon fusion. The gluon emitted by the $c\bar{c}$ state is due to C-parity conservation.*

1.3 Theoretical interests in the J/Ψ study

The production mechanism of quarkonia (bound states of quark - antiquark) is still puzzling. None of the models for quarkonium production at hadron colliders explains successfully both polarization and differential cross section measurements. [15]

Until 1995 the Color Singlet Model (CSM) described successfully the J/Ψ hadroproduction. In this model, the QCD processes were factorized into two parts: the hard parton-parton interaction producing the final partons and the hadronization process. The former can be treated using a perturbative approach and the latter by non-perturbative ones. The point of this model is that the partons produced by the hard scattering must have the same quantum numbers of the initial state (QCD conserves the angular momentum, the parity and the charge conjugation quantum numbers). As the J/Ψ decay requires a three gluon leg Feynman diagram in order to preserve the quantum numbers, the same condition is required for its direct production (see Fig. 1.4). We will refer to this mechanism as direct production of prompt J/Ψ.

The $C = +1$ charmonia production requires instead only two gluons. Therefore one might expect that the J/Ψ is, to a good approximation, not produced directly in hadron-hadron collisions, but arises from decay of charmed quarkonia with even charge conjuga-

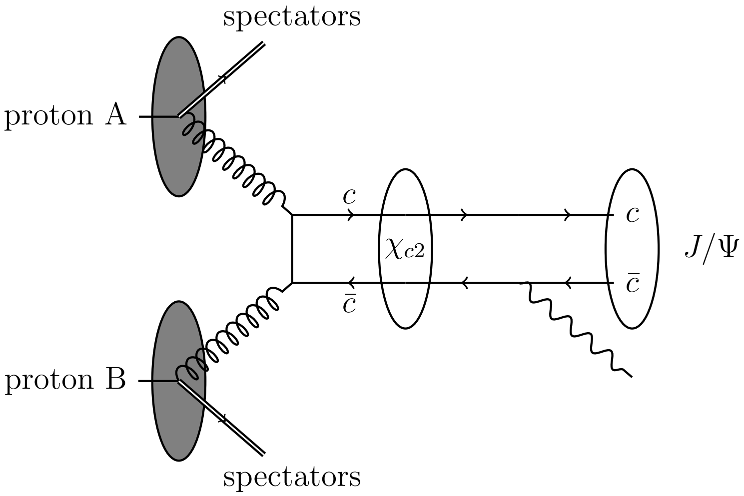

Figure 1.5: *Feynamn diagram of prompt indirect J/Ψ production by gluon-gluon fusion: $g+g \rightarrow \chi_{cJ} \rightarrow J/\Psi+\gamma$*

tion:

$$g+g \rightarrow \chi_{cJ} \rightarrow J/\Psi+\gamma \tag{1.4}$$

Process 1.4 proceeds mostly via χ_{c2} and we will refer to it as indirect prompt J/Ψ production (see Fig. 1.5).

As shown by the inclusive quarkonium cross section data at the Tevatron [16], the CSM underestimates the cross section for prompt J/Ψ production in $p-\bar{p}$ collisions. The Color Octet Mechanism (COM), part of the Non-Relativistic QCD (NRQCD) approach [17], has been able to explain the cross section measurements, but predicts a polarization, which is in contrast with recent data at the Tevatron [18]. According to the COM, the $c\bar{c}$ bound state produced by the hard parton-parton scattering is not required to be directly in a singlet colour state, but it can successively emit low p_T gluons in order to reach such a state. The requirement on color singlet and the co-linearity divergence of the low p_T gluon emission enhances the direct J/Ψ production.

Thanks to the much higher collision energy and luminosity of the LHC, quarkonia can be probed with transverse momenta much higher than currently studied at the Tevatron, allowing us to better discriminate between theoretical models.

In summary, J/Ψ's production at hadron colliders occurs in three ways: prompt J/Ψs produced directly, prompt J/Ψs produced indirectly (via decay of heavier charmonium states such as χ_c), and non-prompt J/Ψs from the decay of a b-hadron.

1.4 Experimental interests in the J/Ψ reconstruction

The J/Ψ particle represents a very useful test for the detector performance. The Compact Muon Solenoid (CMS) experiment is designed for the study of physics events with high transverse energy final state particles. Thus, detector performances are not expected to be optimal for the reconstruction of particles with low p_T. Particularly, the reconstruction of low p_T electrons in CMS is a challenging task, though it could be a crucial point in the discovery of the Higgs boson in the $H \rightarrow ZZ^* \rightarrow 4\ell$ decay channel. We will give more details in Chapter 5. The J/Ψ analysis can be a very useful test for the electron reconstruction efficiencies and detector performances as well. Moreover, the measurement of the peak position of the J/Ψ resonance will be used, combined with the π^0 and the Z boson ones, for the calibration of the CMS electromagnetic calorimeter. The linear response of the calorimeter is then provided in a wide energy range: from the MeV scale of the π^0 to the hundred- GeV scale of the Z boson, through the GeV scale of the J/Ψ particle. Thus, the J/Ψ peak is the intermediate point in the interpolation between π^0 and Z.

Chapter 2

The Large Hadron Collider and the Compact Muon Solenoid detector

2.1 The Large Hadron Collider

The Large Hadron Collider (LHC) construction was approved by the CERN Council in 1994 and started in the late 2000, after the closure of the Large Electron Positron collider (LEP).

The LHC [19] is a circular hadron accelerator designed to accelerate protons at the energy of 7 TeV energy per beam (14 TeV in the center of mass) and ions (Pb) at the energy of 2.76 TeV per nucleon in the center of mass. Up to now, the LHC is the highest energy hadron collider ever constructed and also the biggest one. In order to reach such a high energy, the LHC needs a very big radius tunnel in which particle beams circulate. It is installed in the LEP tunnel situated approximately 100 meters underground between the French and Swiss territory in the Geneva area (see Fig. 2.1). The tunnel is 27 km long. Prior to the injection in the LHC the particles are prepared by

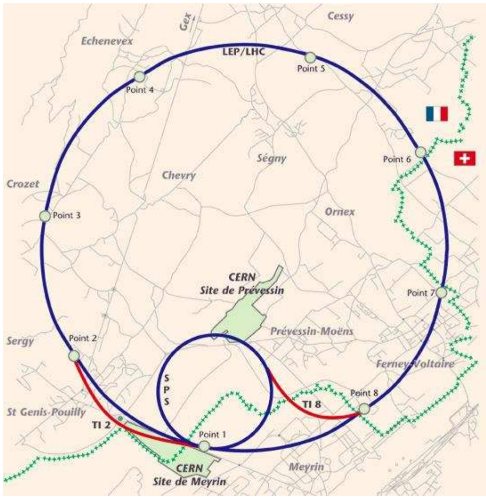

Figure 2.1: *View of the LHC location*

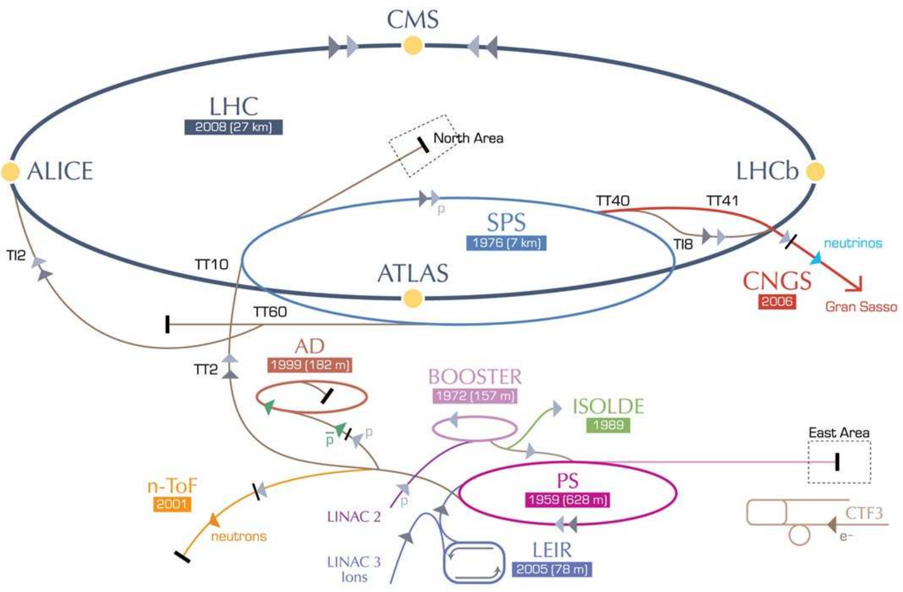

Figure 2.2: *Proton (ions) acceleration and injection system to the LHC: LINAC2, PSB, PS, SPS and LHC*

a series of injective systems that successively accelerate them: the LINAC2, the PSB, the PS (from 1.4 to 26 GeV) and the SPS up to 450 GeV (see Fig. 2.2).

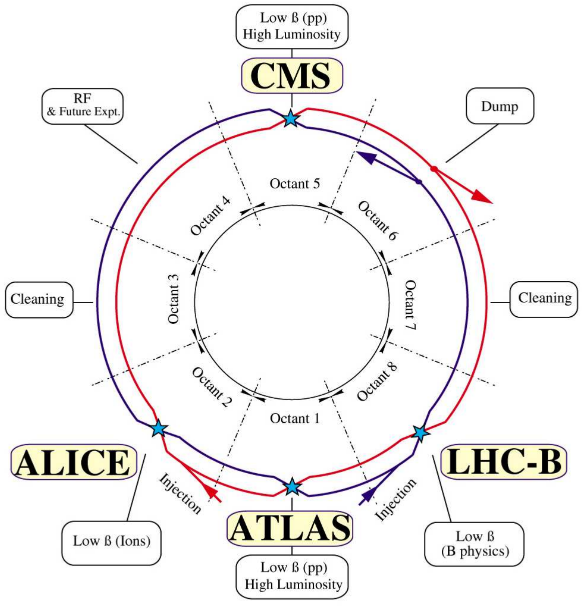

Figure 2.3: *View of the four LHC experiments positions and LHC layout*

The LHC is organized in 8 octants hosting 1600 superconducting magnets operating at a temperature of 1.9 K that allow to maintain the protons on the circular orbit from the injection energy up to the 7 TeV nominal energy and a few RF accelerating sections that accelerate the particles to the nominal energy. The protons in the accelerator are inserted in bunches. Up to 2800 bunches of 10^{10} protons can be inserted in the machine.

The main accelerator characteristics are summarized in Table 2.1.

The experimental caverns are located in

length	27 km
center mass energy	14 TeV
luminosity	10^{34} cm^{-2}s^{-1}
bunches	16
proton per bunch	10^{10}
collision rate	40 MHz
MAGNETS	
number	1600
working temperature	1.9 K
magnetic field	8 T

Table 2.1: *Summary table of design characteristics of the LHC for proton-proton collisions.*

the four points where the two beam pipes intersect to prodce collisions. Four experiments are installed there, with different designs and aims: ALICE for the study of quark-gluon plasma in heavy ion collisions, LHCb for the study of the CP violation in heavy flavour quarks physics (b-quark), ATLAS and CMS, which are two general purpose experiments.

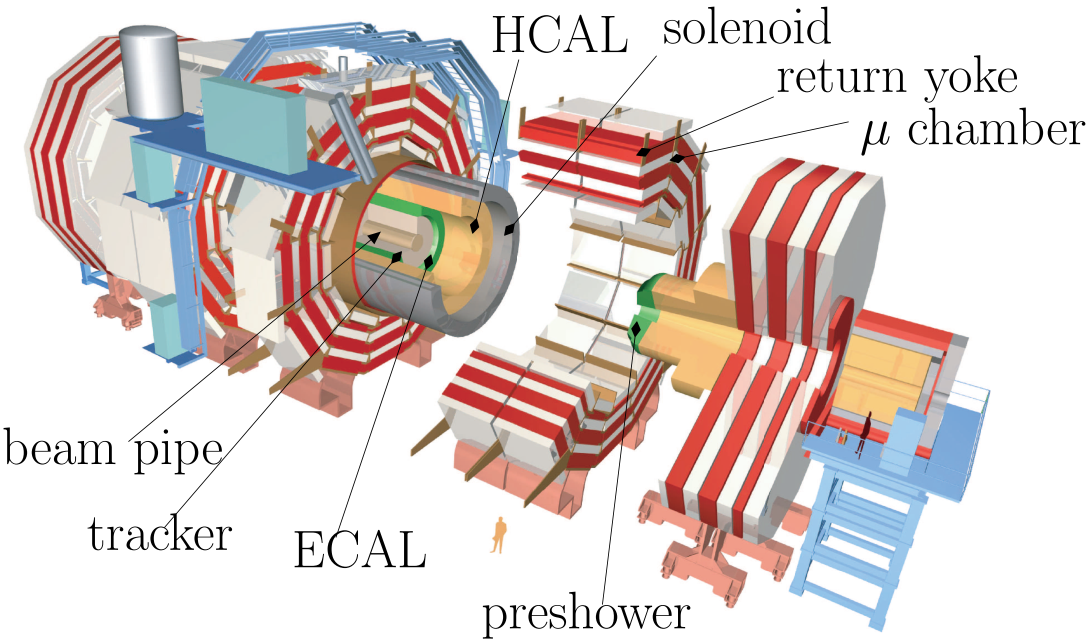

Figure 2.4: *The CMS detector*

2.2 The Compact Muon Solenoid detector

The Compact Muon Solenoid (CMS)[20] experiment (shown in Figure 2.4) is made of a large superconducting solenoid containing a full silicon tracker, a precise crystal electromagnetic calorimeter (ECAL) and a hadron calorimeter (HCAL). Muon chambers are embedded in the iron return yoke of the magnet. Overall the experiment measures 21.6 m in lenght, 14.6 m in height and weighs 12500 t.

As sketched in Fig. 2.5, the combined information from the different subdetectors allows the discrimination of the final stable particles produced by the collision.

We will describe briefly all the subdetectors giving more details on the ones involved in the electron reconstruction (the tracker system and ECAL). An electron releases a little amount of energy in the tracker layers revealed as hits. Because of the bending power of the magnetic field, the electron follows an helix trajectory until the ECAL. It developes in an electromagnetic shower that is almost completely contained in the ECAL crystal length. Thus, almost no signals are released in the HCAL and in the muon chambers.

At the design luminosity, a mean of about 20 inelastic collisions will be superimposed on the event of interest. This implies that around 1000 charged particles will emerge from

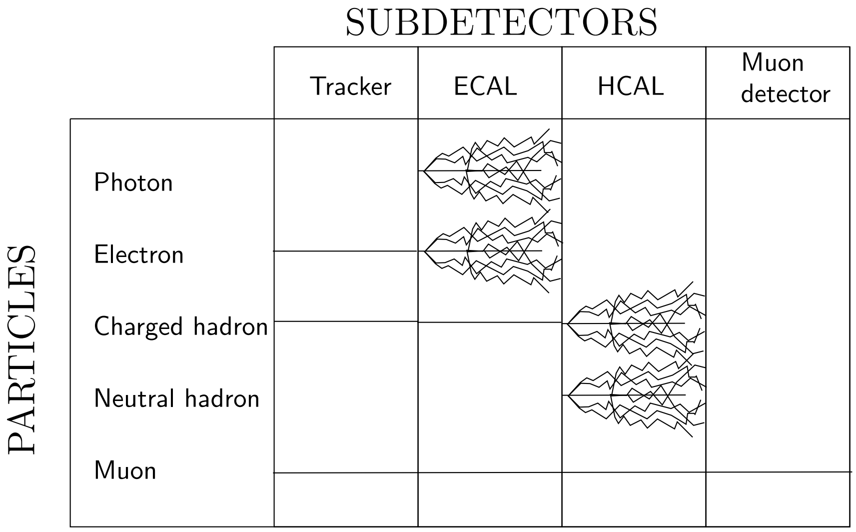

Figure 2.5: *Schematic description of the interaction of the final state particles produced in the collision with the CMS subdetectors. Charged particles are revealed by the tracker as several hits in the different layers. The hits are used to define the particle trajectory. Neutral particles are not seen in the tracker system. Electrons and photons produce electromagnetic showers loosing almost all their energy in the ECAL. Hadrons interact producing hadron showers in HCAL. Muons pass all the subdetectors releasing energy as MIPs.*

the interaction region every 25 ns. The products of an interaction under study may be confused with those from other interactions in the same bunch crossing. This problem becomes more severe when the response time of a detector element and its electronic signal is longer than 25 ns. The effect of this pile-up can be reduced by using high-granularity detectors with good time resolution, resulting in low occupancy. This requires a large number of detector channels. The resulting millions of detector electronic channels require very good synchronization.

2.2.1 The coordinate system

The coordinate system has the origin centered at the nominal collision point inside the experiment, the y-axis pointing vertically upward, and the x-axis pointing radially toward the center of the LHC. Thus, the z-axis points along the beam direction according to the write-hand rule. The azimuthal angle ϕ is measured from the x-axis in the x-y plane and the radial coordinate in this plane is denoted by r. The polar angle θ is measured from the z-axis. Pseudorapidity is defined as $\eta = -\log\left(\tan\frac{\theta}{2}\right)$. Thus, the momentum and energy transverse to the beam direction, denoted by p_T and E_T respectively, are computed from the x and y components. The imbalance of energy measured in the transverse plane is called missing E_T and denoted by $\not{E}_{\mathrm{T}}$.

2.2.2 The magnet

Magnetic length	12.5 m
Cold bore diameter	6 m
Central magnetic induction	3.8 T
Nominal current	19.14 kA
Inductance	14.2 H
Stored energy	2.6 GJ
Operating temperature	1.8 K
Yoke magnetic induction	1.8 T

Table 2.2: *The principal characteristics of the CMS solenoid magnet.*

An important aspect driving the detector design and layout is the choice of the magnetic field configuration for the momentum measurement. Large bending power is needed to measure precisely the momentum of high-energy charged particles since the momentum resolution improves with a stronger magnetic field: the relative uncertainty on the momentum measurement is $\frac{\delta p}{p} \propto \frac{p}{B}$. This forces a choice of superconducting technology for the magnets.

The CMS magnet [21] is a superconducting solenoid providing a 3.8 T magnetic field at the interaction point. The tracker system, ECAL and HCAL are hosted within the magnet.

The magnet return yoke of the barrel has 12-fold rotational symmetry and consist of three sections along the z-axis; each is split into 4 layers (holding the muon chambers in the gaps). Most of the iron volume is saturated or nearly saturated, and the field in the yoke is around 1.8 T.

2.2.3 Tracker system

The silicon tracker [22, 23] is the innermost part of the CMS detector. At design luminosity about 1000 tracks/event are expected, therefore high detector granularity is needed.

Speed and radiation hardness are other two requirements for the tracker because of the high intense flux of charged particle expected by the interactions at the LHC design luminosity. Moreover, the minimum material budget is required in order to keep lower the multiple scattering, photon conversion and bremsstrahlung emission.

In the barrel region the tracking system consists of a cylindrical detector of 5.5 m in length and 1.1 m in radius. It is equipped with 3 silicon pixel detector layers (66 million channels) for the innermost part (for radii 4.4 cm $< R <$ 10.2 cm and for $|z| <$ 50 cm) and 10 silicon strip detector layers (2.8 million channels) for the outer part ($R <$ 110 cm, $|z| <$ 275 cm).

The tracker silicon strip detector consists of four inner barrel (TIB) layers assembled in shells with two inner endcaps (TID), each composed of three small discs. The outer barrel (TOB) consists of six concentric layers. Finally two endcaps (TEC) close off the tracker.The tracker system layout is schematically shown in Fig. 2.6.

The tracker system provides a very precise measurement of particle momentum and is crucial for low p_T electrons.

For high p_T track (100 GeV) the p_T resolution is about $1-2\%$ in the central region and a bit worse in the endcaps due to the lower lever arm. At this p_T the multiple scattering contribution is about $20 - 30\%$ and it increases for lower transverse momentum. The efficiency is above 99% in most of the acceptance. There is a small drop at high η due to the lack of coverage of the pixels.

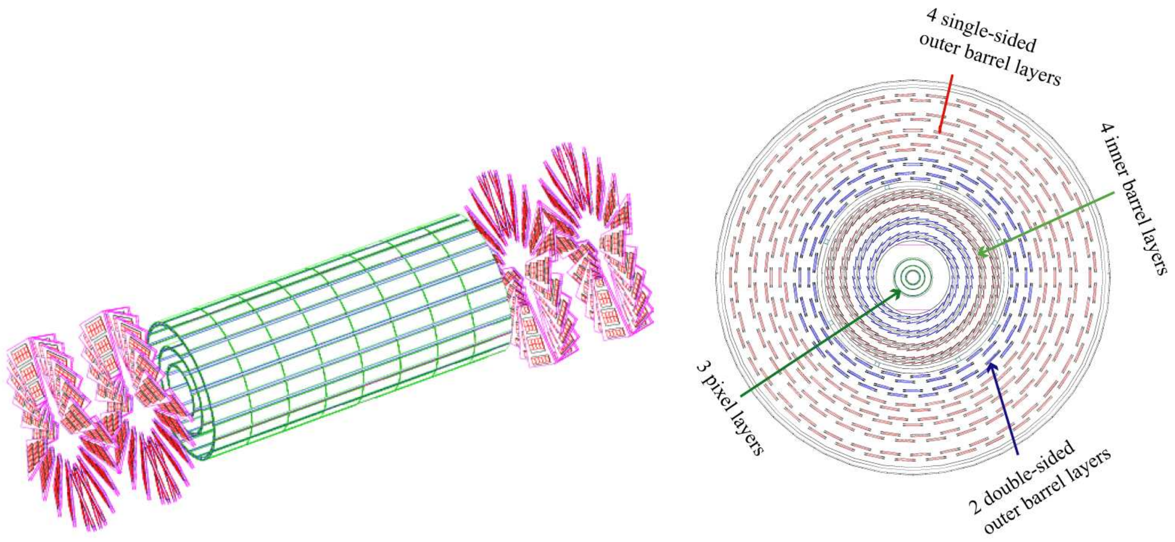

(a) Pixel detector layout (b) Trasversal view of the CMS tracker

Figure 2.6: *a) Layout of the pixel detector in CMS tracker. b) Layout of the barrel tracker.*

Pixel

The pixel system is the closest part of the CMS detector to the interaction region and it's used to reconstruct the primary and secondary vertices. It contributes precise tracking points in $r - \phi$ and z and therefore is responsible for a small impact parameter resolution that is important for good secondary vertices reconstruction.

The pixel detectors provide in general 2 or 3 hits per track, each with a three-dimensional resolution of about 10 μm in the transverse plane and 15 μm in z.

Strip detector

The silicon strip detectors can provide up to 14 hits per track, with a two-dimensional precision ranging from 10 μm to 60 μm in R. Some of the silicon strip layers are double-sided to provide a longitudinal measurement with a similar accuracy. The tracker acceptance for a minimum of 5 collected hits extends up to pseudorapidities η of about $|\eta| < 2.5$.

Material budget

The material thickness in the tracker volume to be traversed by electrons and photons before reaching the ECAL strongly varies with η. It amounts to about 0.35 radiation length (X_0) at central pseudorapidities ($\eta = 0$), increases towards the ECAL barrel/endcap transition, and falls back.

The simulation of the material budget in front of ECAL is of great importance for the estimation of the photon conversion (photons interacting with the tracker material producing an electron-positron pair) both for photon analyses as lost signal and for electron analysis as a background source.

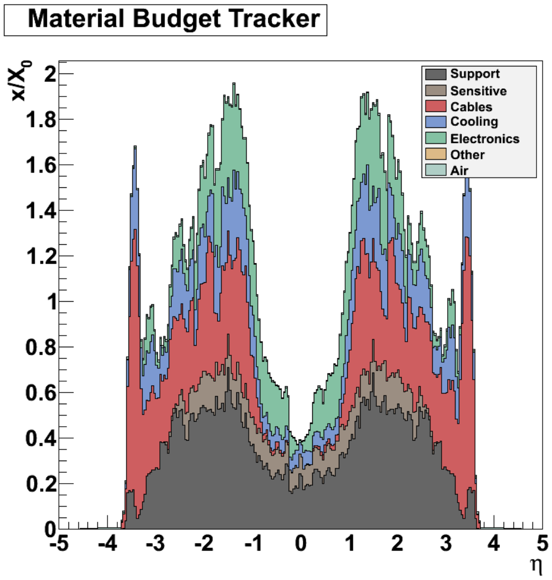

Figure 2.7: *Material budget*

High material budget also means an higher fraction of electron bremsstrahlung.

2.2.4 Electromagnetic Calorimeter

One of the driving criteria in the design of the electromagnetic calorimeter (ECAL) [24, 25] was the capability to detect the decay into two photons of the postulated Higgs boson. This capability is enhanced by the good energy resolution provided by a homogeneous crystal calorimeter.

The CMS ECAL is made of approximately 75000 $PbW0_4$ crystals, a transparent scintillating material denser (8.3 g/cm^3) than iron with a short radiation length ($X_0 = 0.89$ cm) and a small Molière Radius ($\mathrm{R_M} = 2.19$ cm). This allowed to build a fine granularity and a compact calorimeter such that an electro-magnetic shower is completely contained in its 25 X_0.

The scintillation decay time of these crystals is of the same order of magnitude as the LHC bunch crossing time: about 80% of the light is emitted in 25 ns. In order to

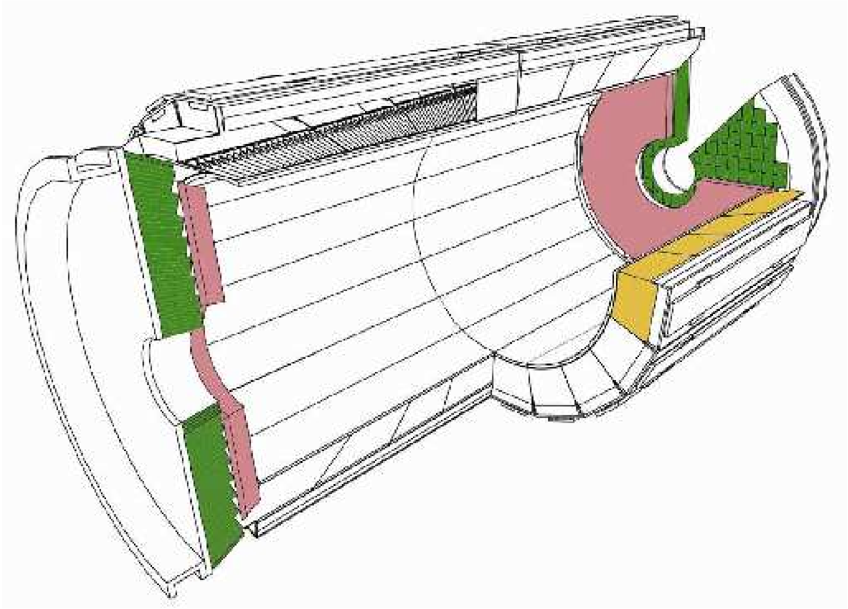

Figure 2.8: *Schematic view of* ECAL *layout*

compensate the low light yield (100 photons per MeV), the lead tungstate crystals are coupled to photodetectors with a high gain: Avalanche Photo-Diodes (APDs) are used in the barrel, characterized by a higher magnetic field, and vacuum phototriodes (VPTs) in the endcaps because insensitive to the high hadron flux.

The CMS ECAL is a hermetic calorimeter consisting in a central cylindrical part (barrel) placed between the tracker and the hadron calorimeter and closed by two endcaps. A preshower detector is placed in front of the endcap crystals.

The ECAL layout is shown in Fig. 2.8.

The ECAL Barrel

The ECAL Barrel covers the region $|\eta| < 1.479$. The barrel is made of 61200 trapezoidal and quasiprojective crystals of approximately 1 Molière Radius ($\mathrm{R_M}$) in lateral size and about $25.8\,X_0$ in depth. The barrel inner radius is of 124 cm.

Viewed from the nominal interaction vertex, the individual crystals appear tilted (off-pointing) by about 3° both in polar (η) and azimuthal angles (ϕ). The barrel is divided in two halves, each made of 18 supermodules containing 1700 crystals.

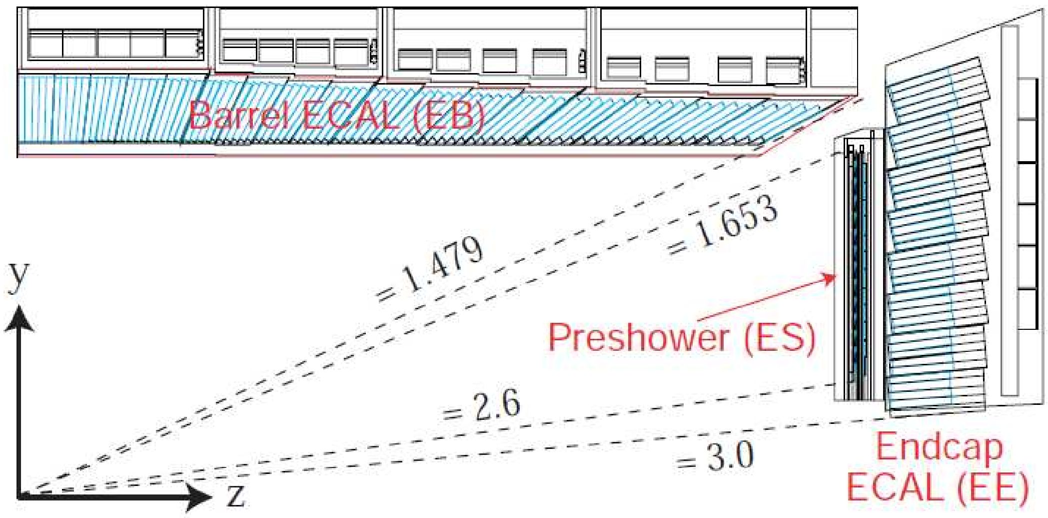

Figure 2.9: *Schematic view of ECAL layout*

The ECAL Endcap

The endcaps consist of two detectors, a preshower device followed by a $PbW0_4$ calorimeter (Fig. 2.9). The preshower is made of silicon strips placed in a 19 cm sandwich of materials including about $2.3\,X_0$ of Pb absorber. It covers inner radii from 45 cm to 123 cm, corresponding to the range $1.6 < |\eta| < 2.6$. Each endcap calorimeter is made of 7324 rectangular and quasi-projective crystals of approximately 1.3 R_M in lateral size and about $24.7\,X_0$ in depth. The crystal front faces are aligned in the (x, y) plane but, as for the barrel, the crystal axes are off-pointing from the nominal vertex in the polar angle by about 3°.

ECAL energy resolution

The energy resolution of the ECAL can be parametrized as follows:

$$\left(\frac{\Delta E}{E}\right)^2 = \left(\frac{S}{\sqrt{E}}\right)^2 + \left(\frac{N}{E}\right)^2 + C^2 \tag{2.1}$$

The stochastic term S depends on event to event fluctuations in lateral shower containment, photo-statistics and photodetector gain; N represents the noise term, which depends on the level of electronic noise and event pile-up (additional particles causing signals that overlap in time); and C represents the constant term, which depends mainly on intercalibration, temperature, high voltage stability and other system intrinsics and also on

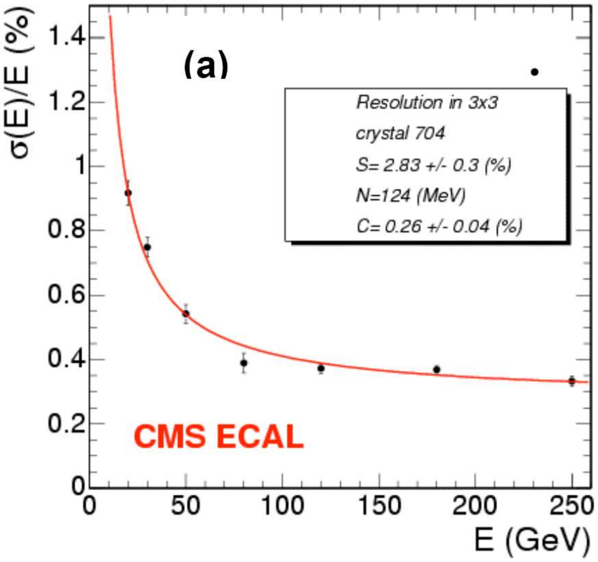

Figure 2.10: *Energy resolution of ECAL barrel as a function of the energy for the* 3×3 *array of crystals centered on crystal 704.*

non-uniformity of the longitudinal light collection and leakage of energy from the rear face of the crystal. The constant term dominates the resolution at high energies.

The mean value of the stochastic and constant term in the barrel was measured in test beam [26]: $S = 2.8\%$, $N = 124$ MeV and $C = 0.3\%$.

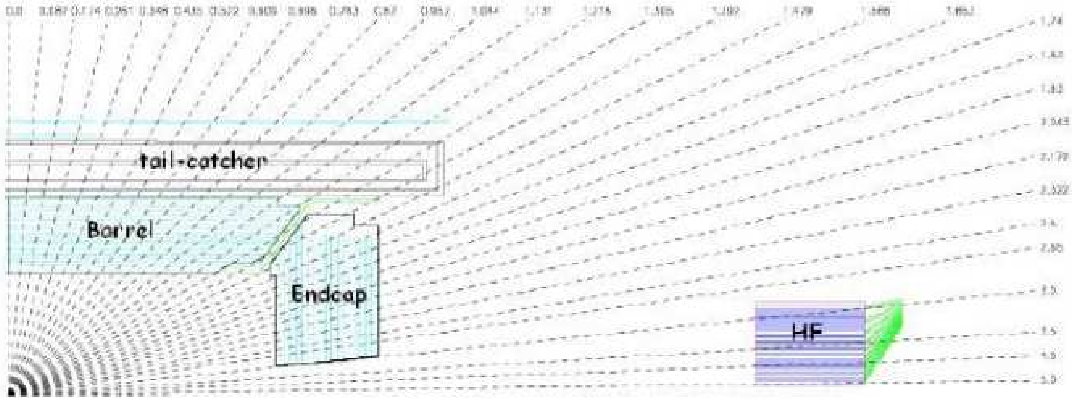

Figure 2.11: *Longitudinal view of the CMS hadron calorimeter. The HCAL covers up to* $|\eta| < 5$.

2.2.5 Hadron Calorimeter

The hadron calorimeter (HCAL) [27] is used together with ECAL to measure energy and direction of jets, and the energy imbalance in the transverse plane $\not{E}_{\mathrm{T}}$. It provides good segmentation, moderate energy resolution and angular coverage up to $|\eta| < 5$. HCAL is made of four subdetectors (Fig. 2.11):

- the Barrel Hadronic Calorimeter (HB) is placed inside the magnetic coil and it covers the central pseudorapidity region, up to $|\eta| = 1.3$
- the Endcap Hadronic Calorimeter (HE) is inside the magnetic coil as well and it is made of two endcaps extending the angular coverage up to $|\eta| = 3$
- the Outer Hadronic Calorimeter (HO, or Tail Catcher) is placed in the barrel region, outside the magnetic coil and is needed to enhance the depth of the calorimeter in terms of nuclear interaction length λ
- the Forward Hadronic Calorimeter (HF) consists of two units placed outside the magnetic coil, at ±11 m from the interaction point along the beams direction. It extends the pseudorapidity coverage up to $|\eta| = 5$.

HB and HE are made with layers of $4 \div 7.5$ cm thick brass or stainless steel absorber plates interleaved with 3.7 mm thick plastic scintillators. The signal is readout through wavelengthshift fibres and hybrid photodiodes (HPD). The granularity ($\Delta\phi \times \Delta\eta$) is

0.087×0.087 in the central part and 0.17×0.17 at high η. The minimum depth is about $5.8\,\lambda$. In order to increase the calorimeter depth in the barrel region a tail catcher (HO) has been added outside the magnetic coil. HO is made of two scintillator layers, with the same granularity as HB; the total depth in the central region is thus extended to about $11.8\,\lambda$, with an improvement in both linearity and energy resolution. HE has a minimum depth of $10\,\lambda$. The two HFs are made of steel absorbers with embedded radiation hard quartz fibers. The fast Cherenkov light produced is collected with photomultipliers. The granularity is 0.175×0.175.

HB has an energy resolution for single pions of approximately $120\%/\sqrt{E}$.

The energy resolution of the ECAL-HCAL combined system was evaluated with a combined test beam with high energy pions [28] and it is given by:

$$\frac{\Delta E}{E} = \frac{84.7\%}{\sqrt{E}} \oplus 7.4\%$$

2.2.6 The muon system

The CMS muon system [29] is dedicated to the triggering, identification and momentum measurement of high $p_T$muons, the latter in combination with the tracker. The system is placed outside the magnetic coil, embedded in the return yoke, to fully exploit the 1.8 T return flux. The system consists of three independent subsystems (Fig. 2.12(a)):

- Drift Tubes (DT) are choosen for the barrel region, where the occupancy is relatively low (< 10 Hz/cm^2), the magnetic field uniform and the hadron flux low;
- Cathode Strip Chambers (CSC) are used in the endcaps, where the occupancy is higher (> 100 Hz/cm^2);
- Resistive Plate Chambers (RPC) are both in the barrel and in the endcaps.

The Drift Tube system is made of chambers consisting of twelve layers of drift tubes each, packed in three independent substructures called super-layers, for a total of four chambers with three super-layers per chamber. In each chamber two super-layers have anode wires parallel to the beam axis, and one has perpendicular wires. Thus, each chamber can provide two measurements along the $r - \phi$ coordinate and one measurement

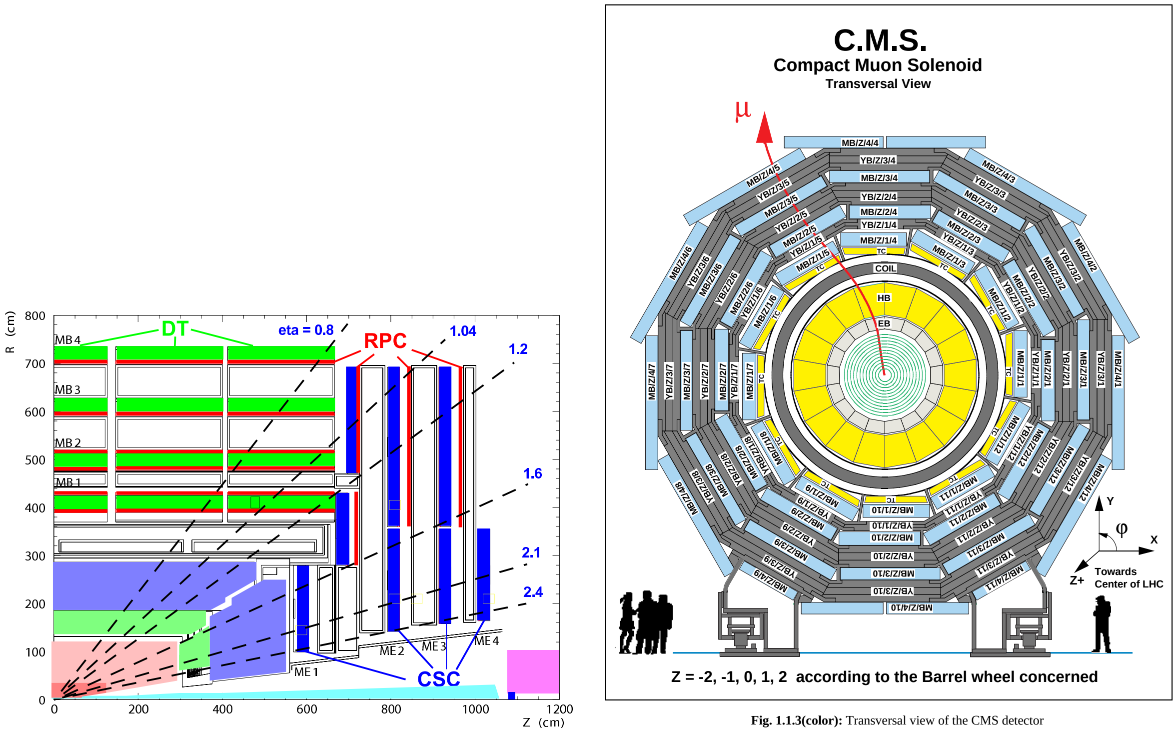

(a) Longitudinal view

(b) Trasversal view

Figure 2.12: *Longitudinal and trasversal view of the CMS muon system*

along z. Each chamber is made of two parallel aluminium plates jointed with "I" shaped spacer cathodes. Chambers are filled with a gas mixture of Ar(85%) and CO_2(15%). The position resolution is about 100 μm in both $r - \phi$ and rz.

Cathode Strip Chambers are multi-wire proportional chambers with segmented cathodes. Each chamber can provide both hit position coordinates. Chambers are filled with a gas mixture of Ar(40%), CO_2 (50%), CF_4(10%). The chamber spatial resolution is about $80 - 85$ μm.

Resistive Plate Chambers are made of parallel bakelite planes, with a bulk resistivity of $10^{10} \div 10^{11}$ Ωcm. They are operated in avalanche mode. These chambers have limited spatial resolution, but they have excellent timing performances; they are used for bunch crossing identification and for trigger purposes.

2.3 The CMS Trigger

At design luminosity LHC will provide a bunch crossing every 25 ns corresponding to a frequency of 40 MHz. It is not possible to store the huge amount of data coming from the million electronic channels of the detector for all the interactions. Only 200 MB/s of data can be stored on disks nowadays and since the typical CMS event data size is $1 - 2$ MB, approximately $100 - 200$ Hz can be accepted. The largest part of events are minimum bias events, which have a cross section of about 70 mb $\sqrt{s} = 7$ TeV, which has to be highly suppressed. In order to do this, CMS implements a two stage trigger: the Level 1 (hardware) trigger (L1) and the Higher Level (software) Trigger (HLT). The L1 trigger consists of custom designed, largely programmable electronics, taking information directly from subdetectors and provided a reduction of event rate of about 1000. The HLT is a software system implemented in a filter farm of about one thousand commercial processors running a software event filter that is a faster version of the offline reconstruction algorithms. The HLT provides a reduction of the event rate to about 100 Hz.

The trigger flow is shown in Fig. 2.13.

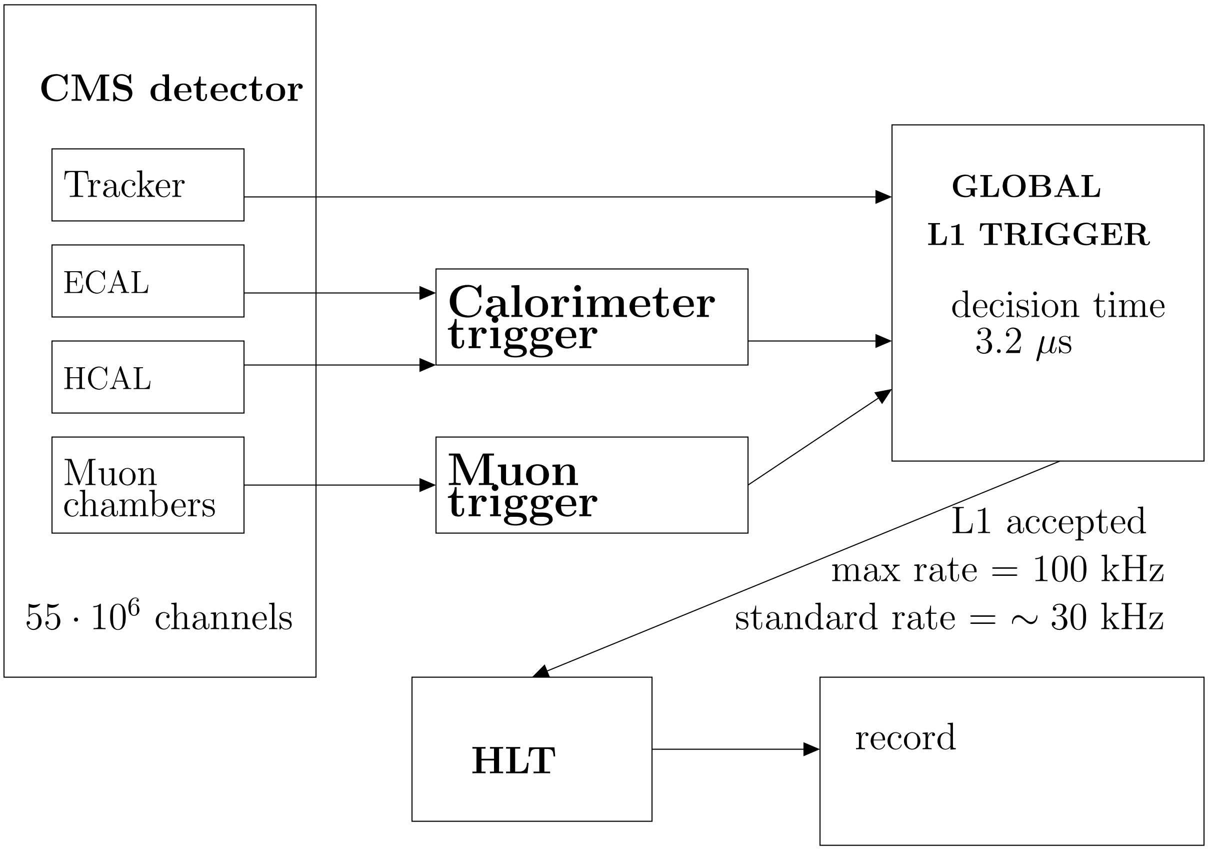

Figure 2.13: *Workflow of the CMS trigger system*

Chapter 3

Electron reconstruction

3.1 Electron definition and reconstruction

Electrons can be reconstructed as energy deposit in ECAL with an associated track. The direction of the electron is given by the tangent to the track at the vertex, while the energy is a linear combination of the momentum estimated by the track and the energy deposit in ECAL (a detailed description is provided in Sec. 3.2).

The CMS detector is equipped with a very accurate electromagnetic calorimeter and silicon tracker. The reconstruction and identification of electrons is nevertheless a challenging task. Indeed, the large amount of tracker material (from $0.4\,X_0$ at $\eta = 0$ to a maximum of $1.4\,X_0$ at $\eta = 1.5$, as shown in Fig. 2.7) induces a significant bremsstrahlung photon emission, which, because of the track curvature in the 3.8 T magnetic field, can result in a calorimeter energy deposit widely spread in the azimuthal direction (ϕ).

In the CMS reconstruction software (CMSSW) the electron reconstruction procedure is divided into steps [30]:

1) electron seeding

2) electron tracking

3) electron preselection (track - ECAL matching)

4) Bremsstrahlung recovery

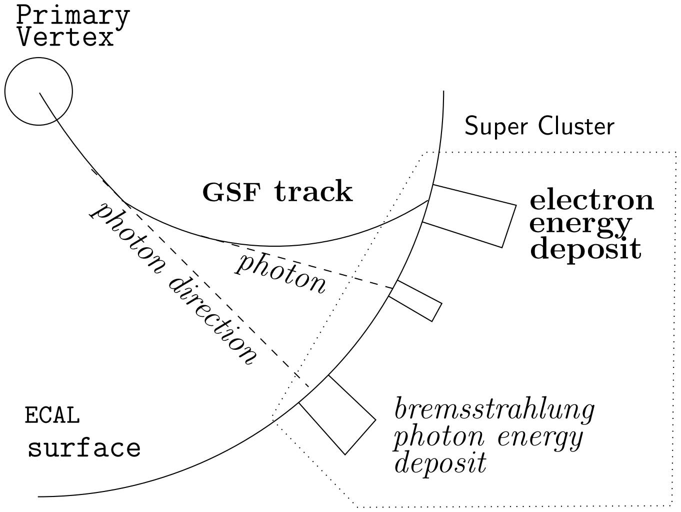

Figure 3.1: *Schematical view of an electron reconstructed in CMS. The track is reconstructed by the GSF algorithm taking into account the trajectory kinks due to energetic bremsstrahlung photon emission. The energy deposits belonging to the emitted photons are collected together to the electron cluster by the clustering algorithm.*

3.1.1 Track reconstruction

The Kalman Filter (KF) algorithm [31] is the standard track reconstruction algorithm in CMS. It was developed for MIP like muons and is the faster track algorithm. Because of the bremsstrahlung emission, electron track reconstruction needs a dedicated tracking algorithm that can take into account the kinks given by the bremsstrahlung energy loss to the electron direction, this is the GSF track algorithm [32] (see Fig. 3.1).

3.1.2 Electron seeding

In CMS there are two electron reconstruction algorithms which differ by the seeding procedure: EcalDriven electrons [33] (inward procedure starting from ECAL and associating then a track) and TrackerDriven electrons [34] (outward procedure starting from a track and searching energy deposits in ECAL).

The EcalDriven algorithm is the standard CMS electron reconstruction, most suitable for energetic and isolated electrons. Low-energy (below 10 GeV) and/or non-isolated electrons, are reconstructed more efficiently by the TrackerDriven electron algorithm.

Electron seeds selected by both algorithms are collected together, keeping track of the seeding algorithm originating them. In the following we will refer to TrackerDriven and EcalDriven electrons as those seeded by the TrackerDriven and EcalDriven algorithm respectively.

EcalDriven algorithm

The EcalDriven approach starts finding suitable energy deposits in the ECAL. The 97% of the impinging electron energy is deposited in a cluster of 5×5 crystal matrix around the most energetic one (called seed crystal). Such simple fixed size array of crystals has been shown to allow for best energy resolution for electrons in test beam and unconverted photons in situ.

To obtain a measurement of the electron energy at primary vertex and minimize the cluster containment variations, it is essential to collect bremsstrahlung photons. This is the purpose of the super-clustering algorithms. In the barrel Super Clusters (SCs) are obtained grouping together "dominoes" of 3 or 5 crystals in η contiguous in ϕ, until a domino with less than 100 MeV is reached. In the endcaps they are obtained grouping 5x5 clusters along the ϕ direction.

Super Clusters are firstly preselected applying a threshold of 4 GeV on the deposited tranverse energy and an hadronic veto. The veto is defined by the ratio between the hadronic and the SC energy ($H/E < 0.15$). The hadronic energy is estimated by summing HCAL towers energy within a cone of $\Delta R = 0.15$[1)] behind the Super Cluster position.

Hit pairs and triplets in the pixel layers constitute a trajectory seed. The trajectory seeds in a z and ϕ window along the electron helix trajectory starting from the SC are selected as geometrically matching trajectory seeds. The ϕ matching is performed propagating the SC ϕ direction backward to the first pixel layers using both charge hypotesis.

[1)] $\Delta R = \sqrt{\Delta\eta^2 + \Delta\phi^2}$

TrackerDriven algorithm

The TrackerDriven algorithm follows the so called "particle flow" procedure [35]. The Particle Flow algorithm aims at reconstructing all the individual particles in jets by making an optimal combination of the different sub-detectors. In the case of an electron, it implies reconstructing the track up to the ECAL entrance, associating this track with the electron cluster, and identifying the clusters of the emitted photons.

The KF algorithm fails to reconstruct the track of highly bremsstrahlung emitting electrons. On the other hand, the GSF algorithm is about 10 times slower than the KF one. Thus, in the particle-flow, the seeding efficiency is increased by a pre-identification procedure [36] schematically shown in in Fig. 3.2.

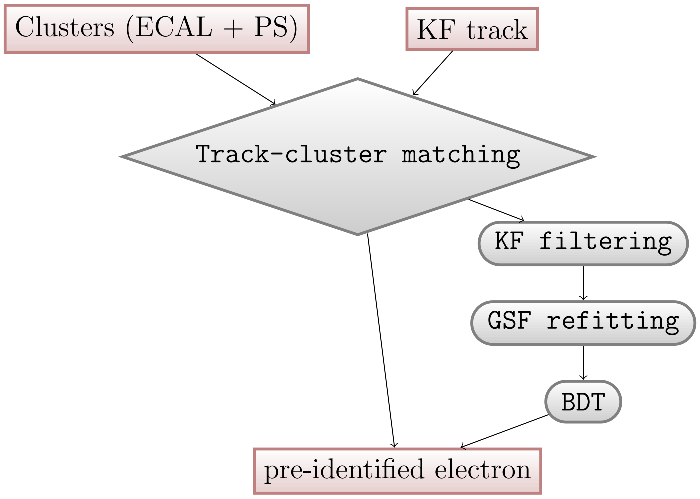

Figure 3.2: *Electron pre-identification strategy*

The electron pre-identification starts from the tracks. A high tracking efficiency is thus required, even for tracks with a small number of hits. An iterative-tracking strategy was adopted to achieve both high efficiency and low fake rate [37].

The electron which do not loose too much energy by Bremsstrahlung are the easiest to identify. Indeed the KF can follow their trajectory from the interaction point to the outermost layer of the tracker and they can be easily associated to a ECAL cluster; for this reason the first pre-identification criterion is based on track-cluster matching. The KF track (with at least ten hits) is propagated to the internal surface of the ECAL. The propagator used does not take into account possible energy losses and considers an uniform

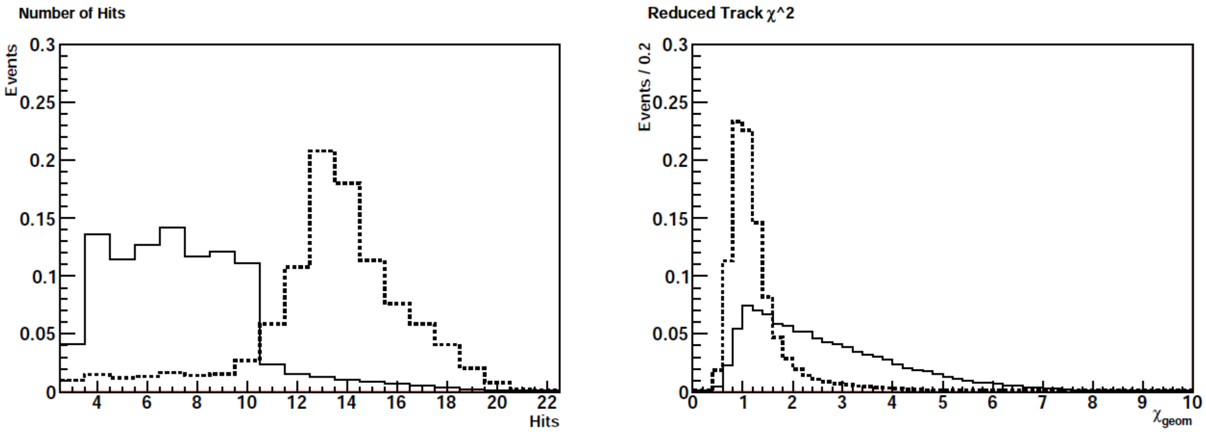

Figure 3.3: *Distribution of the number of hits (left) and χ^2_{KF}/ndf (right) for electrons (solid line) and pions (dottendd line).*

magnetic field. After reaching the internal ECAL surface, the track is propagated with a straight line to the depth where the electron shower maximum is expected. For all the clusters verifying the condition $\frac{1}{3} < \left|\frac{E_{cl}}{P_{tk}}\right| < 3$, the most geometrically compatible one is associated to the track. The compatibility is evaluated building a χ^2 variable:

$$\chi^2_{geom} = \left(\frac{\Delta\phi}{\sigma_\phi}\right)^2 + \left(\frac{\Delta\eta}{\sigma_\eta}\right)^2$$

where $\Delta\phi(\eta)$ is the distance in $\phi(\eta)$ between the position of the cluster and the position of the propagated track and $\sigma_{\phi(\eta)}$ is the intrinsic cluster position resolution.

After finding the best matching, two variables are used to select the electrons for which the photon emission is small: low χ^2 and a not small ratio between the cluster energy and the absolute value of the track momentum at the outermost layers ($E_{cl}/\left|P_{tk}\right|$).

All the tracks not selected by the first criterion are filtered using two KF criteria: a little number of hits and a big value of the reduced χ^2 of the track (see Fig. 3.3).

This filter is expected to be fully efficient for electrons and to reduce, at least, by a factor two the hadrons. The main reason of this stage is to reduce the number of charged hadrons for the following analysis which is the most time-consuming. The filtered KF tracks are then refitted using a GSF model in order to improve the discriminating power of the pure-tracker variables used in a MultiVariate Analysis based on a Boosted Decision Trees (BDT). A decision tree is a sequence of binary splits of the data. To train the tree a set of known training events is used. The results are measured using a separate set

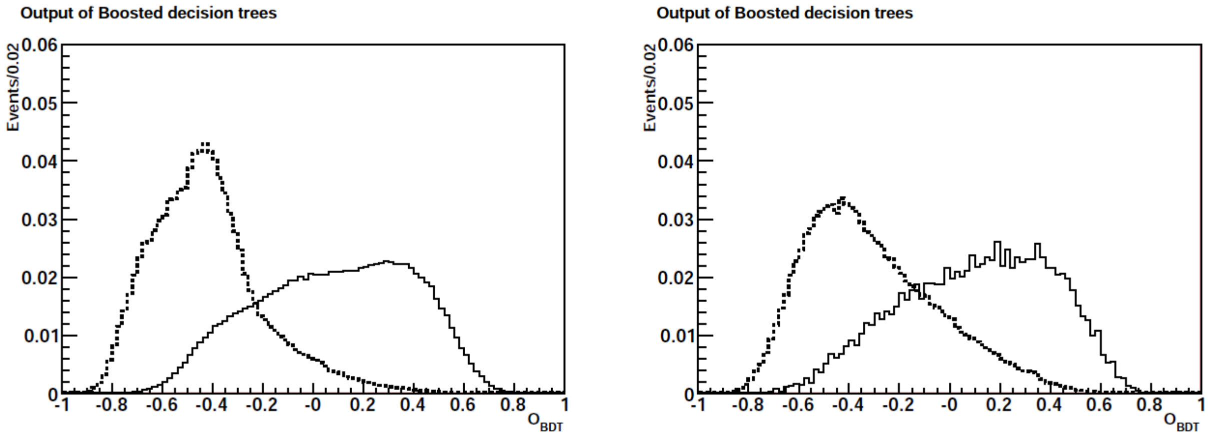

Figure 3.4: *BDT output normalized distribution for electrons (solid line) and pions (dotted line) for single particles (left) with* 2 GeV/$c < p_T <$ 50 GeV/c*, for particles in jet (right) in the same* p_T *range.*

of known testing events. Consider all of the data to be on one node. The best variable value to split the data into separate signal and background is found. There are then two nodes. The process is repeated on these new nodes and is continued until a given number of final nodes (called “leaves”) are obtained, or until all leaves are pure or until a node has too few events. [38]. The input variables used in the BDT are: E/p, χ^2_{ECAL}, Number of hits per track, $|p_T^{out} - p_T^{in}| / p_T^{in}$, χ^2_{GSF}, χ^2_{KF}/χ^2_{GSF}, p_T and η. The output of the BDT is one variable (O_{BDT}) that permits to discriminate electrons and hadrons (see Fig. 3.4).

3.1.3 Electron tracking

The seeds obtained with the TrackerDriven and EcalDriven procedures are merged in order to provide a unique collection of seeds keeping track of the seed origin. Electron seeds are then used to initiate a dedicated electron track building and fitting procedure in order to best handle the effect of bremsstrahlung energy loss. The track finding is based on a combinatorial KF, requiring a very loose χ^2 compatibility. The combinatorics is limited by requiring at most 5 candidate trajectory at each layer and at most one layer with a missing hit. The hits collected by the track finding are then fitted by the GSF.

When an EcalDriven seed, with N hits, and a TrackerDriven seed share at least N-1 tracker hits, only the former is kept and the provenance is assigned to both algorithms.

3.1.4 Electron preselection

EcalDriven

As far as EcalDriven electrons, the GSF track-ECAL matching requires:

- $|\Delta\eta_{in}| = |\eta_{\text{SC}} - \eta_{in}^{extr}| < 0.02$
- $|\Delta\phi_{in}| = |\phi_{\text{SC}} - \phi_{in}^{extr}| < 0.15$

where η_{SC} and ϕ_{SC} are the energy weighted position of SC in η and ϕ respectively and where η_{in}^{extr} and ϕ_{in}^{extr} are the η and ϕ coordinate position of the closest approach to the SC position, extrapolating from the innermost track position and direction.

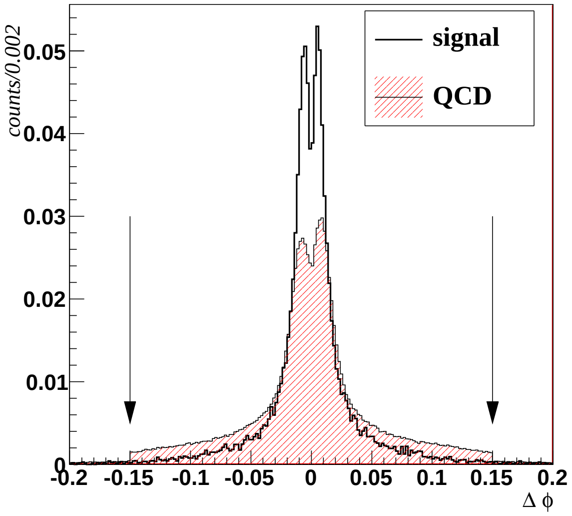

Figure 3.5: *Normalized to unity $\Delta\phi$ shapes for J/Ψ and QCD MC samples. The double peak is due to the charge hypotesis.*

TrackerDriven

A GSF track is linked to a given cluster if the extrapolated position from the outermost tracker measurement in the calorimeter is within the boundaries of one of the cells constituting the cluster.

For TrackerDriven electrons, a further step is the electron identification. It consists of a multivariate analysis based on the BDT on variables different respect to the pre-identification phase. The multivariate analysis takes into account variables related to the bremstralung emission, the electromagnetic shower shape, the number of hits, the χ^2 of the GSF and KF track fit in order to maximize the electron pre-identification efficiency and the hadron rejection.

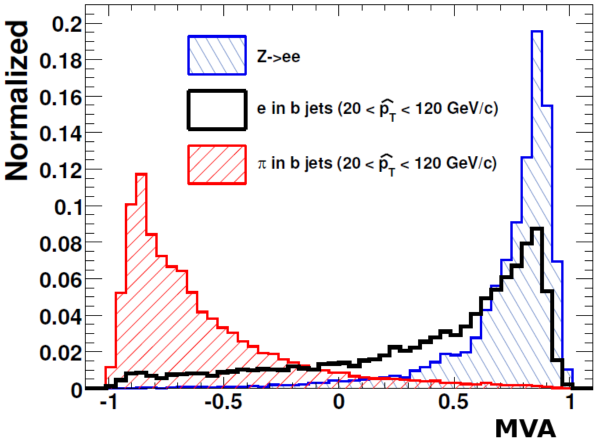

Figure 3.6: *MVA distribution for Z electrons, electrons in b-jets and pions in b-jets*

.

The BDT output is the so called MVA (MultiVariate Analysis) variable.

Electron candidates with $MVA > -0.4$ are selected. Fig. 3.6 shows the distribution of the MVA variable for electrons and pions.

3.1.5 Removal of Conversions from Bremsstrahlung Photons

Once preselected, a further selection step is applied to remove ambiguous electron candidates that arise from the reconstruction of conversion legs from photon(s) radiated by primary electrons. In the case of an emitted photon taking more than half of the original electron p_T, the predicted position in the next layer is closer to the photon than to the electron after emission. If the photon converts, the hits from its conversion legs will likely be efficiently found by the electron track reconstruction algorithm. In such bremsstrahlung conversion patterns, the reconstruction often leads to electron candidates constituted by closeby tracks associated to the same or closeby superclusters, hereafter defined as ambiguous candidates.

The ambiguity solving algorithm firstly identifies electron candidates having superclusters “in common”. Therefore, two superclusters are considered “in common” if a minimum energy is shared. Having identified candidates with common supercluster, the ambiguity resolution algorithm keep the electron candidate satisfying the first of the following creteria:

1) the innermost first hit

2) the best E/p ratio

3.2 Energy measurement and resolution

The electron energy is obtained from the combination of the ECAL and the tracker measurements, so to take advantage of the better resolution of the ECAL at high energies and the better resolution of the tracker momentum estimation at low energies. Indeed, the electron p_T resolution, as estimated from the trajectory curvature in the tracker, get worse with the increasing electron transverse momentum:

$$\frac{\delta p_T}{p_T} \propto p_T \tag{3.1}$$

The relative resolution of the electron energy as estimated by ECAL, instead, increases with the electron energy as in Eq. 2.1

So the combination of the two measurements takes advantage of the track momentum estimate in particular in the low energy region and/or in the ECAL crack regions.

The single and combined energy resolution in ECAL Barrel (EB) is shown in Fig. 3.7(a); the combined p_T resolution for barrel and endcaps is shown in Fig. 3.7(b).

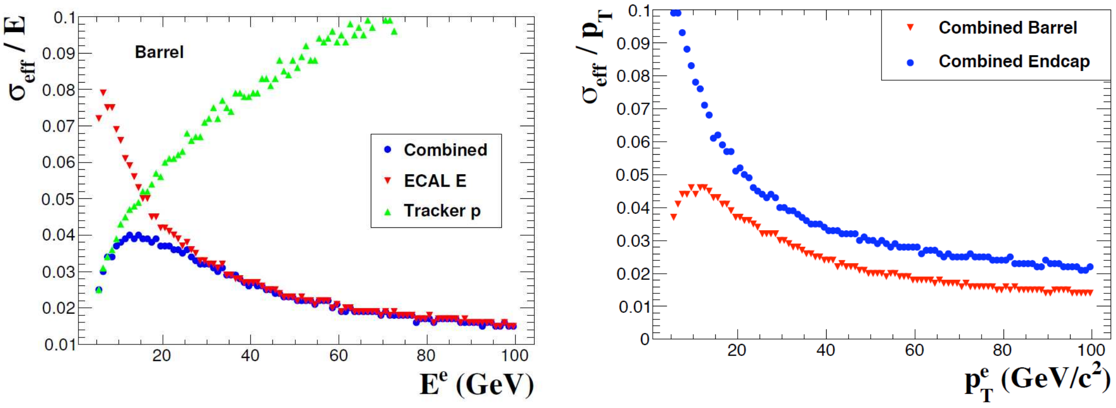

(a)

(b)

Figure 3.7: *Performances of the combined momentum estimate: (a) effective energy resolution for the ECAL, the tracker and the combined momentum estimates as a function of the electron generated energy for electrons in the ECAL Barrel and (b) effective transverse momentum resolution for electrons in the ECAL Barrel and electrons in the EE. Electrons are from a sample of di-electron events with uniformly distributed transverse momentum between 2 and 150 GeV/c.*

Chapter 4

Selection of $J/\Psi \rightarrow e^+e^-$ events

This chapter illustrates in details the selection to extract a clean sample of $J/\Psi \rightarrow e^+e^-$ events.

We will follow all the analysis steps starting from a study of simulated signal and background events until the definition of the best J/Ψ selection procedure.

The study of events with the first data of the CMS experiment is complicated by the increasing luminosity provided by the LHC and the consequently changing trigger configuration.

4.1 MC events simulation

In modern high energy physics experiments, a key role is played by Monte Carlo (MC) simulations. They are used especially to better understand the collision dynamics and the detector response to final state particles. In this way, any New Physics (NP) evidence can be disentangled from known physics and detector effects. In fact, the whole event is simulated starting from the parton-parton fundamental interaction (generation step) up to the interaction of final state particles with the matter of the detector (simulation step). The simulated detector information is then processed by the CMS reconstruction framework (CMSSW) as the real data are.

The generation step may be performed by different event generators which use different algorithms and theorical informations. The one used in this analysis is PYTHIA [39].

The simulation step is performed using a full simulation of the CMS detector based on GEANT4 [40, 41]. Since the simulation step is the most time consuming, after the generation step the events are passed through an event filter rejecting unuseful or undetecteble events. Only the events passing the event filter are then simulated.

In this work, we will use the MC samples to choose an adequate selection for the interesting events (signal) able to reject as much as possible background events. Given the non perfect simulation of low p_T processes and the reduced knowledge of the detector conditions in this early data-taking era, we will try to rely as less as possible on MC simulations, using data-driven methods.

MC normalization

In order to get an estimation with good precision of the expected number of events in an integrated luminosity $\mathcal{L}_{int}$, the MC sample must contain a large number of simulated events, corresponding at least to the same order of magnitude of the analyzed data.

The equivalent integrated luminosity of the sample is defined by

$$\mathcal{L}_{eq} = \frac{N}{\sigma \cdot \epsilon}$$

where N is the number of events generated and simulated for that sample, σ is the process cross-section and ϵ is the MC filter efficiency.

4.1.1 Signal MC sample

The signal MC sample is generated by PYTHIA 6 requiring events with prompt J/Ψ decaying into electrons according to the combination of the CSM and the COM (see Sec. 1.3).

Two signal MC datasets were produced. The first one (we will refer to it as signal_1) requires looser conditions on the decay electrons and it was used in order to choose the J/Ψ selection cuts. It was produced simulating the older J/Ψ trigger. The second one (we will refer to it as signal_2) was produced simulating the last J/Ψ dedicated trigger adopted in CMS (it will be described in Sec. 4.3.3). In Sec. 5.4 we will present the cross section measurement of the prompt J/Ψ production in proton-proton collisions for J/Ψ

with rapidity[1] $|y| < 1.4$ and $p_T > 4$ GeV. These requirements are choosen for the comparison of the measurement with the muon channel decay performed in CMS. The signal_2 sample was produced with those cuts at generator level on the J/Ψ rapidity and transverse momentum. It will be used for data-MC comparisons and efficiency studies for the J/Ψ cross section measurement (Sec. 5.4).

The event filter selection on generated quantities is:

1) signal_1

   - two electrons with opposite charge
   - both J/Ψ electrons with $p_T > 1.5$ GeV/c
   - both J/Ψ electrons with $|\eta| < 2.5$ (in the detector geometrical acceptance)

2) signal_2

   - two electron with opposite charge
   - J/Ψ with transverse momentum $p_T > 4$ GeV/c
   - J/Ψ with rapidity $|y| < 1.4$

The MC sample characteristics are reported in Tab. 4.1.

4.1.2 Background Monte Carlo sample

Signal events with electrons in the final state are contaminated by a background stemming mainly from QCD di-jets in which at least one of the jets has been revealed as a well-isolated single electromagnetic (EM) cluster. The cluster is caused mainly by energetic (single or multiple) π^0, η, K_s^0 mesons decaying into photons in the final state (with following possible conversion of the photon to an e^+e^- pair) as well as by $\pi^\pm$ and $K^\pm$. As a rule these background particles are accompanied by soft hadrons whose energy is

---

[1] Rapidity is defined as:

$$y = \frac{1}{2} \log \frac{E + p_z c}{E - p_z c}$$

Signal_1	
Prompt $J/\Psi \to e^+e^-$ cross section (σ)	12.5458 μb
Filter efficiency (ϵ_{MC})	0.0352
Effective cross section ($\sigma \cdot \epsilon_{\mathrm{MC}}$)	$4.4 \cdot 10^5$ pb
Equivalent integrated luminosity ($\mathcal{L}_{eq}$)	1.4 pb^{-1}
Signal_2	
Prompt $J/\Psi \to e^+e^-$ cross section (σ)	12.5458 μb
Filter efficiency (ϵ_{MC})	0.024
Effective cross section ($\sigma \cdot \epsilon_{\mathrm{MC}}$)	$3.0 \cdot 10^5$ pb
Equivalent integrated luminosity ($\mathcal{L}_{eq}$)	3.3 pb^{-1}

Table 4.1: *Main characteristics of signal MC samples*

mostly deposited around the one of the fake electron. In most cases it is not possible to completely suppress all background events, and the fraction of the remaining events has to be evalueted.

In order to generate a sufficiently large sample of QCD di-jets in a p_T range which is representative of the background for a di-electron selection in a reasonable time, a generator-level preselection algorithm is needed to "enrich" the QCD sample with electrons.

Thus, the more realistic QCD background MC sample available for the $J/\Psi \to e^+e^-$ study is represented by the QCD Double Electro Magnetic Enriched (QCDDoubleEMEnriched) sample. The specific filter before the simulation requires the presence in the event of at least two particles that can produce an energy deposit in the ECAL sufficient to mimic an electron (i.e. "fake electrons") or QCD jets containing b and c quark decaying into real electrons.

The QCDDoubleEMEnriched sample requirements at generator level are:

- at least two particles with $E^T > 4$ GeV$/c$ in the detector acceptance $|\eta| < 2.5$

At the moment of the writing QCDDoubleEMEnriched samples for a complete J/Ψ study are not yet available.

This sample has been used only for a preliminary study on the possible selection strategy, but no selection optimization and efficiency study was possible because of the lack of statistics and the requirements at generation level that make the sample not very representative of the full background.

The QCDDoubleEMEnriched MC sample was produced separately for two p_T ranges as reported in Tab. 4.2.

At the moment of writing there were no QCDDoubleEMEnriched samples simulated with the final trigger described (see Sec. 4.3.3).

QCD EMDoubleEnriched p_T $6 \div 20$	
QCD cross section (σ)	$2.08 \cdot 10^{10}$ pb
Filter efficiency ($\epsilon_{\rm MC}$)	0.02
Effective cross section ($\sigma \cdot \epsilon_{\rm MC}$)	$4.16 \cdot 10^{8}$ pb
Equivalent integrated luminosity ($\mathcal{L}_{eq}$)	0.021 pb^{-1}
QCD EMDoubleEnriched p_T $20 \div \infty$	
QCD cross section (σ)	$2.97 \cdot 10^{8}$ pb
Filter efficiency ($\epsilon_{\rm MC}$)	0.24
Effective cross section ($\sigma \cdot \epsilon_{\rm MC}$)	$7.1 \cdot 10^{7}$ pb
Equivalent integrated luminosity ($\mathcal{L}_{eq}$)	0.154 pb^{-1}

Table 4.2: *Main characteristics of the QCD MC samples*

4.2 Low p_T electron physics

The CMS experiment is designed for the best performances in the study of high p_T physics, i.e. the processes with a hard parton parton scattering resulting in final state particles with high transverse energy.

As shown in Fig. 4.1(a), the prompt J/Ψ particle has, a low p_T spectrum, reflected also by the decay electrons (see Fig. 4.1(b)).

One of the main difficulties of this analysis is triggering low p_T electrons from J/Ψ decays in high luminosity conditions, due to the high rate of background processes. This is

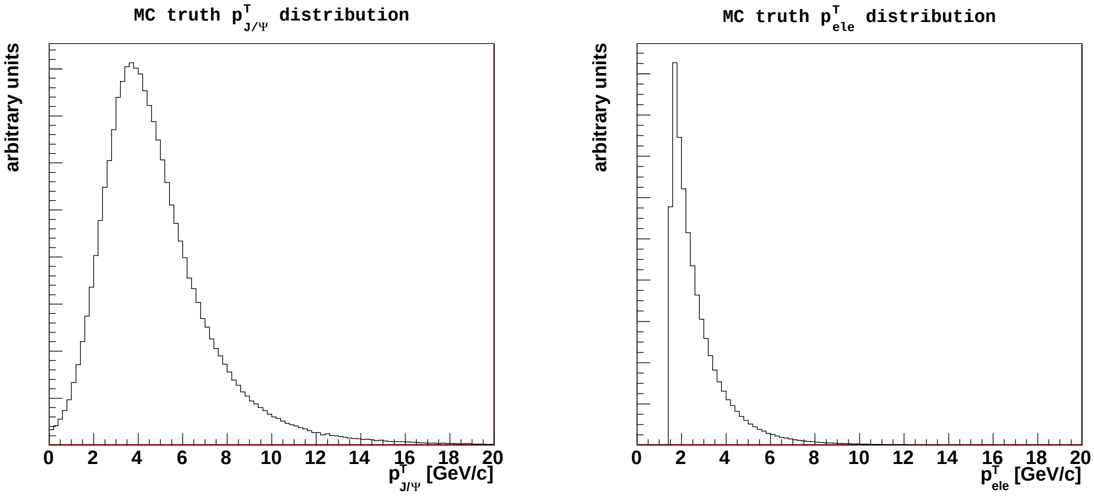

(a) J/Ψ's p_T spectrum (b) J/Ψ's electrons p_T spectrum

Figure 4.1: *Transverse momentum distribution of prompt J/Ψ particle produced at the LHC (left) p_T spectrum of the J/Ψ's decay electrons from MC truth (right). The cut-off at* 2 GeV *in the electron p_T distribution is due to the cut at generator level applied for the signal_1 MC sample production.*

described in Sec. 4.3.3. Futhermore, also the electron reconstruction and identification is more difficult than the high p_T electron case. Different techniques, devoted to this physics case, have been developed. The background coming from fake electrons reconstructed in QCD di-jets is very large, due to the very high cross section of this process. This requires a dedicated optimization of electron identification.

4.3 Event selection

4.3.1 Strategy

In order to keep the background contamination as low as possible without loosing too many signal events, we apply a selection procedure to each electron in the event.

The selection procedure consists of several requests on reconstructed electrons aimed to reject the "fake" electrons (coming from mis-identified hadrons, mainly charged pions or charged hadrons, or neutral pions within the jet with a wrongly-associated track).

The event selection steps are the following:

1) good run (on data only)
2) dedicated HLT trigger path fired
3) number of reconstructed electrons ≥ 2
4) selection cuts applied on each electron
    1) kinematic selection
    2) electron identification
    3) electron isolation
5) oppositly charged electron pair selection
6) if more then two electrons pass the previous criteria, the highest p_T electron pair is choosen

The number of signal_2 MC events passing the selection criteria of step 1) - 4) is the 41% of the total. Since the 0.07% of them has at least 2 electron pairs, the criterium choosen for step 5) is not relevant. Also in data, it represents a negligible fraction of events (0.4%).

4.3.2 Good runs

In CMS the data taking is divided in runs, which last typically 1-10 hours, depending on the detector conditions and LHC fill duration. Not all runs taken by CMS can be used for this analysis, we choose the ones where all the subdetectors involved in the electron reconstruction were up and running in good conditions during the data taking. Up to the end of August the CMS experiment collected 1.8 pb^{-1} of good run data.

4.3.3 J/Ψ dedicated trigger description and performance

The first limitation for the J/Ψ analysis comes from the trigger. Trigger menus are designed to retain events interesting for the LHC physics program, which is selecting high p_T particles on a huge amount of low p_T ones. As already pointed out in Sec. 4.2, leptons from J/Ψ decays are characterized by a low p_T spectrum, with most of them below 10 GeV.

Thus, a dedicated trigger has been implemented with the lowest p_T threshold and other specific requirements in order to keep the highest efficiency according to the bandwidth limits.

From its start up, the LHC increased its instantaneous luminosity of about four orders of magnitude. This means that the amount of interactions arising from the collisions increased considerably. So, different J/Ψ triggers were adopted during different luminosity phases.

For this reason trigger studies were performed choosing the lowest p_T threshold combined with specific selection cuts in order to reject most of the background. These dedicated J/Ψ triggers changed with the increasing of luminosity because of the limited event rate dedicated to this channel by the trigger system.

The J/Ψ triggers implemented up to now are:

HLT_DoublePhoton4_JPsi requires two energy deposits in ECAL with $E^T > 4$ GeV, with a cluster shape compatible with a electro-magnetic shower (details in Sec. 4.3.5) and invariant mass between 2 and 15 GeV

HLT_DoubleEle_4 requires two energy deposit in ECAL with $E^T > 4$ GeV, a track associated to each energy deposit, with a cluster shape compatible with a electromagnetic shower (details in Sec. 4.3.5) and invariant mass between 2 and 15 GeV

The list of J/Ψ dedicated triggers with the reference of integrated luminosity is illustrated in Tab. 4.3.

trigger name	**integrated luminosity**	rate [Hz]
HLT_DoublePhoton4_JPsi	73.5 nb$^-$1	78
HLT_DoublePhoton4_JPsi prescaled (by factor 20)	96.6 nb$^-$1	4
HLT_DoubleEle_4	1.8 pb$^-$1	1

Table 4.3: *J/Ψ trigger table indicating the corresponding integrated luminosity of data collected and the rate expected for an instantaneous luminosity of* $2 \cdot 10^{30}$ cm^{-2} s^{-1}.

In an intermediate period, because of the higher event rate due to the increasing of luminosity, the HLT_DoublePhoton4_JPsi trigger was prescaled by a factor of 20, i.e. only 5% of events firing the trigger were recorder.

In this work we will use the first dataset for the selection optimization described in Sec. 4.5.2. The last dataset was splitted into two parts, one used for the selection efficiency measurement described in Sec. 5.4.2 and the other used for the cross section measurement.

Within a good run we select only the events firing the trigger path chosen for this analysis.

4.3.4 Kinematic selection

As described in Sec. 4.3.3, the HLT requests two energy deposits in the ECAL with trasverse energy $E_T > 4$ GeV. Because of this request, we will apply offline the same request $p_T > 4$ GeV/c on each single electron.

Fig. 4.2 shows the contribution of the different electron reconstruction algorithms to the electron p_T distributions of signal and background. A very large fraction of the signal events are reconstructed by the TrackerDriven algorithm (described in Sec. 3.1.2). The EcalDriven algorithm (described in Sec. 3.1.2) starts reconstructing electrons with $p_T > 4$ GeV/c. The double peak visible in Fig. 4.2(b) is due to both the EcalDriven reconstruction threshold and the generator level cuts of the background sample ($E_T >$ 4 GeV).

The electron energy distribution for the signal is well below the HLT threshold and consequently most of the signal events are not even triggered. On the other hand, also the background (Fig. 4.2(b)) shows a large fraction of events at low p_T and this is the

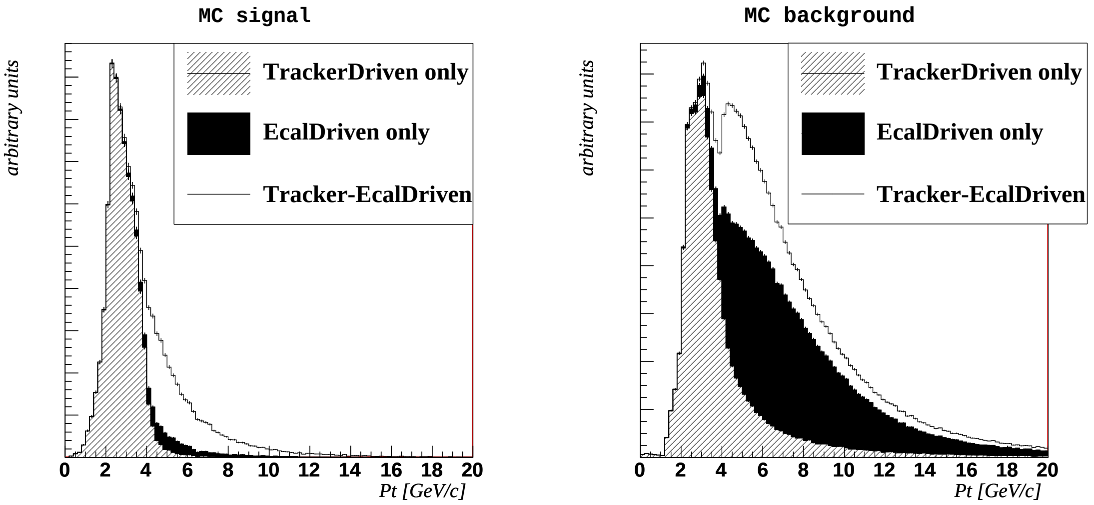

(a) signal MC (b) background MC

Figure 4.2: *Electron p_T distribution for the signal_1 MC sample (4.2(a)) and the background MC sample (4.2(b)). The contributions from the different electron reconstruction algorithms are shown: TrackerDriven only electron (pattern fill), EcalDriven only electrons (black solid fill), electrons reconstructed by both algorithms (white solid fill).*

	J/Ψ events
EB-EB	82%
EB-EE	4%
EE-EE	14%

Table 4.4: *Fraction of reconstructed J/Ψ events from signal_1 MC sample requiring only the HLT and $p_T > 4$ GeV/c. The number of J/Ψ events is divided into three categories: two electrons in the ECAL Barrel (EB-EB), two electrons in the ECAL Endcap (EE-EE), one electron in ECAL Barrel and one in the ECAL Endcap (EB-EE).*

main reason of such a request at trigger level.

As shown in Tab. 4.4 there is a little fraction of signal events with both electrons reconstructed in the endcap region. The tight criteria used to reject the higher amount of background make this fraction negligible. Thus, the following analysis and plots are related to events with two electrons in the barrel region.

4.3.5 Electron identification selection

The electron identification exploits the characteristics of the electron interaction with the detector.

In the following a list of the variables with a brief description and their distribution for the MC signal and the MC background samples are reported (Fig. 4.3, Fig. 4.4, Fig. 4.5, Fig. 4.6, Fig. 4.7). Tight criteria on electron identification variables allow a considerable reduction of "fake" electrons.

H/E It is the ratio of the energy deposit in the HCAL and in the ECAL. The ECAL energy is the energy of the seed; the HCAL energy is estimated in a cone of radious $R = 0.15$ centered to the ECAL seed. Electrons are electromagnetic objects and, as described in 2.5, loose almost all their energy in the ECAL. In order to reject hadrons, a low value of the H/E variable is required. In our analysis the H/E cut ($H/E < 0.1$) is applied to both TrackerDriven and EcalDriven electrons. The cut-off at 0.15 shown in Fig. 4.3 is due to the EcalDriven reconstruction algorithm pre-selection cut. The bin at 0 is due to the HCAL readout threshold.

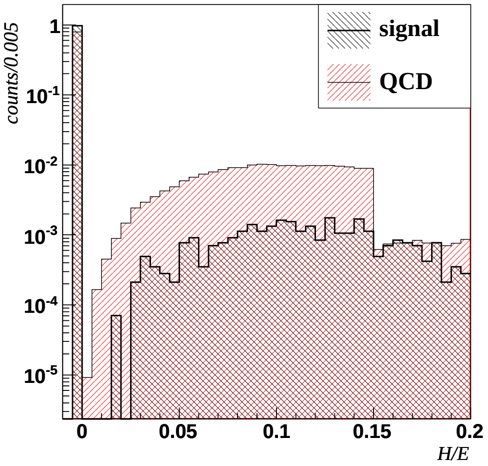

Figure 4.3: *Normalized to unity H/E shapes for signal and background MC samples*

E/p **EcalDriven electron variable.** It is the ratio between the energy deposit in the seed cluster of ECAL and the momentum of the associated track estimated at the end of the track. Because of this choice, the E/p variable is almost insensitive to possible bremsstrahlung emission along the trajectory.

The E/p distribution for electrons is expected to peak at 1 and presents long tails due to the not perfect electromagnetic shower containment in the seed cluster on the left side and to the possible under-estimation of the track momentum for the right tail. Fake electrons, as pions starting their hadronic shower in ECAL, loose only a little part of their energy in ECAL, so a value less than 1 is expected.

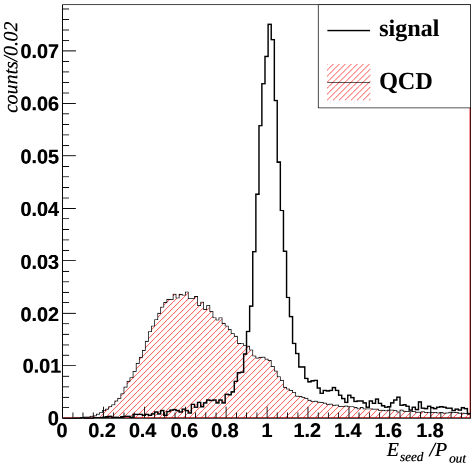

Figure 4.4: *Normalized to unity E/p distributions for signal and background MC samples*

$\Delta\eta$ **EcalDriven electron variable.** It is the difference between the pseudorapidity measured from the track and the one measured by the ECAL both extrapolated at the interaction point. Real electrons are expected to have $\Delta\eta$ close to 0. This variable is not influenced by the bremsstrahlung photon emission because the electron bending occurs in the ϕ direction. The cut-off at $|\Delta\eta| = 0.02$ is due to cuts applied in the reconstruction algorithm. (see 3.1.2).

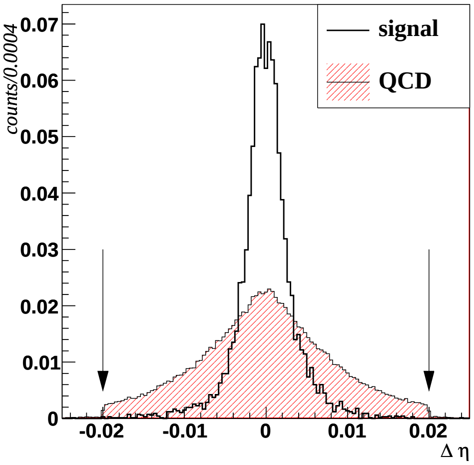

Figure 4.5: *Normalized to unity $\Delta\eta$ distributions for signal and background MC samples*

$\sigma_{\eta\eta}$ **EcalDriven electron variable.** This variable represents the second moment of the cluster shape along the η direction, not affected by the bremsstrahlung emission. The seed of the Super Cluster is considered here. An hadronic shower starting in ECAL shows a distribution larger than the electromagnetic one.

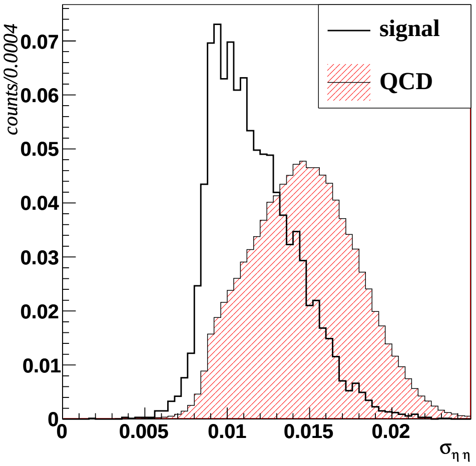

Figure 4.6: *Normalized to unity $\sigma_{\eta\eta}$ distributions for signal and background MC samples*

MVA **TrackerDriven electron variable.** It is a non linear combination of the above mentioned observables and other ones that makes optimal usage of the correlation between the electron identification variables (which in pratice are highly non linear). In the TrackerDriven electron reconstruction a pre-selection cut at -0.4 is applied.

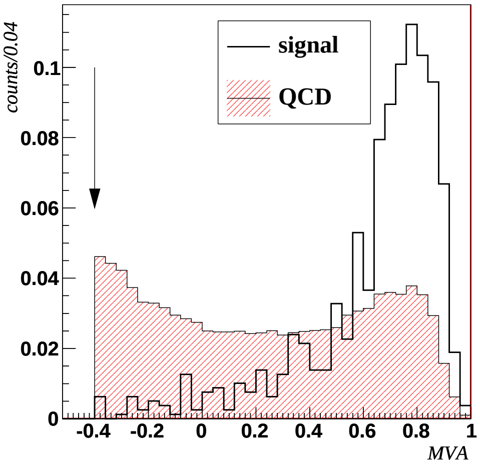

Figure 4.7: *Normalized to unity MVA distributions for signal and background MC samples*

4.3.6 Isolation selection

In this analysis we request isolated electrons in order to reduce the amount of “fake” electrons coming from hadronic jets. Being in jets this kind of clusters are however not isolated. So isolation criteria enhance the prompt J/Ψ contribution.

Isolation criteria can be applied in every subdetector related to the electron reconstruction: tracker, ECAL, HCAL.

Isolation definition:

The isolation variable for an electron in a subdetector can be defined as the flux of energy in a defined cone surrounding it in which we have subtracted the electron contribution.

For the considered electron, we define two concentric cones of radius R_1[2] and R_2 ($R_1 > R_2$) respectively, both centered on the electron direction. The smaller cone is called veto-cone and we make use of it instead of removing just the energy flux contribution of the electron to deal with bremsstrahlung photons as well.

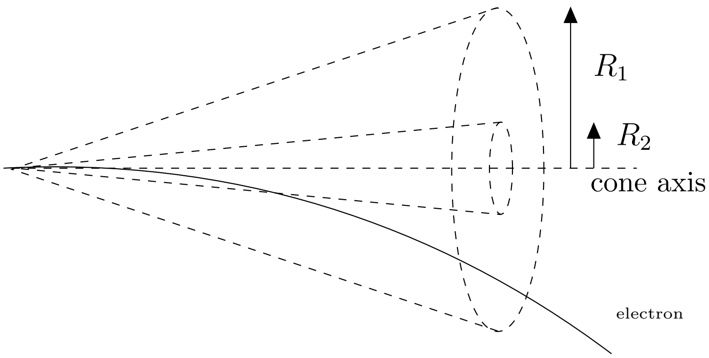

Figure 4.8: *Schematic draw of the isoTk cones.*

Most of the transverse energy measured in the inner cone is due to the electron transverse energy and the transverse energy difference (ΔE^T_{cone}) between the two cones is due to other particles surrounding the electron.

The three isolation criteria applied in this analysis are:

tracker isolation (*isoTk*): We define the electron direction as the one estimated at vertex by the track. The outer and inner cone are choosen with radius $R_1 = 0.3$ and $R_2 = 0.015$ respectively according to optimization studies reported in [42]. The energy flux is the sum of the p_T of particles between the two cones;

---

[2] $R = \sqrt{\Delta\eta^2 + \Delta\phi^2}$

ECAL isolation (*isoECAL*)**:** we make use of the fine granularity of ECAL selecting the cones on a RecHit basis: we define the outer cone of radius $R_1 = 0.3$ and the inner cone of radius R_2 corresponding to 3 crystals around the seed of the SC. A threshold to the RecHit energy of 80 MeV is also applied in order to remove noise contribution to the E^T sum in the isolation variable. In the *isoECAL* definition, in addition to the inner veto-cone removal, there is a a narrow strip in the ϕ direction veto-region that takes into account the spread in the ϕ direction due to the bremsstrahlung emission and to the electrons produced by photon conversions;

HCAL isolation (*isoECAL*)**:** for isolation in HCAL we sum the transverse hadronic energy deposited in towers surrounding the electrons candidate without any threshold, but with a veto-cone around the ECAL position of the electron. The inner cone radius R_2 is fixed to 0.15 in order to make the HCAL isolation variable indipendent to the H/E cut imposed during the electron reconstruction and identification (see Sec. 3.1.2).

The isolation variable distributions are shown for MC signal and background in Figg. 4.9 and 4.10.

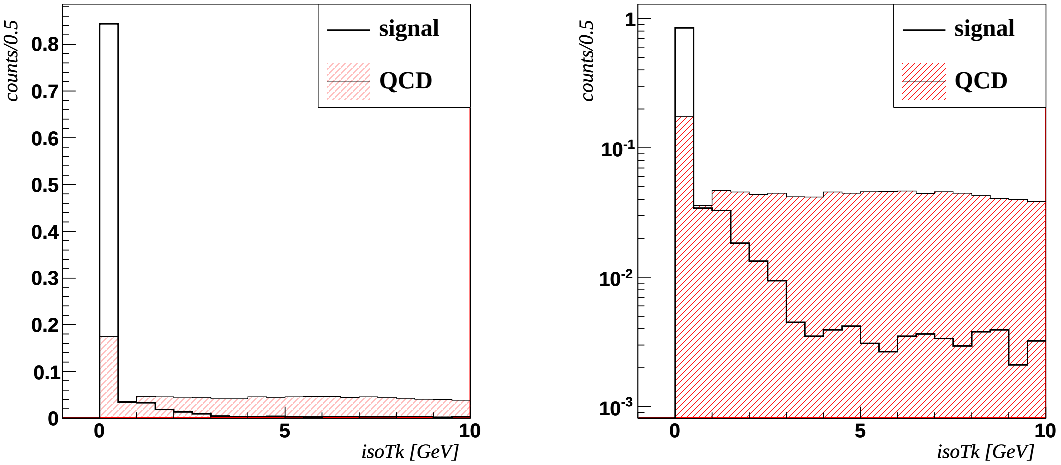

(a) tracker isolation

(b) tracker isolation

Figure 4.9: *Tracker isolation variable (isoTk) distribution for MC signal (white fill) and MC background (filled pattern) in linear a) and logarithmic scale b).*

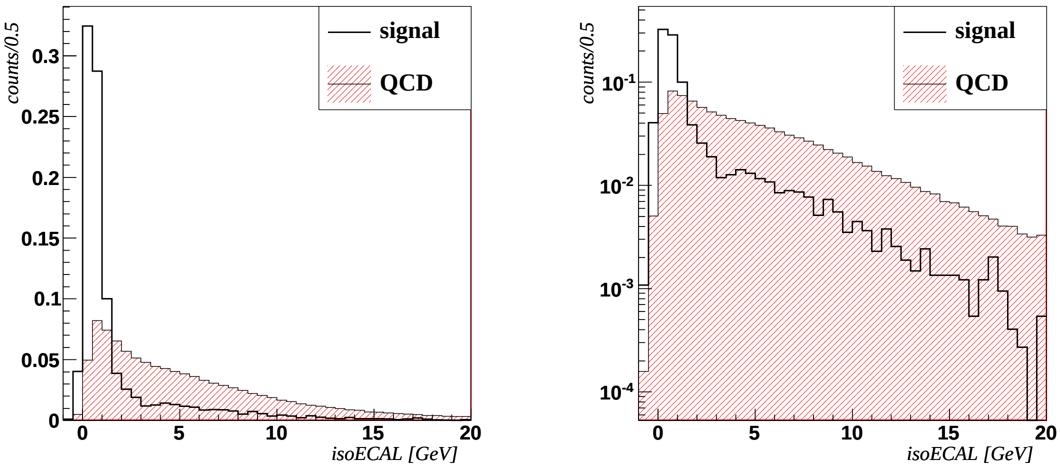

(a) ECAL isolation (b) ECAL isolation

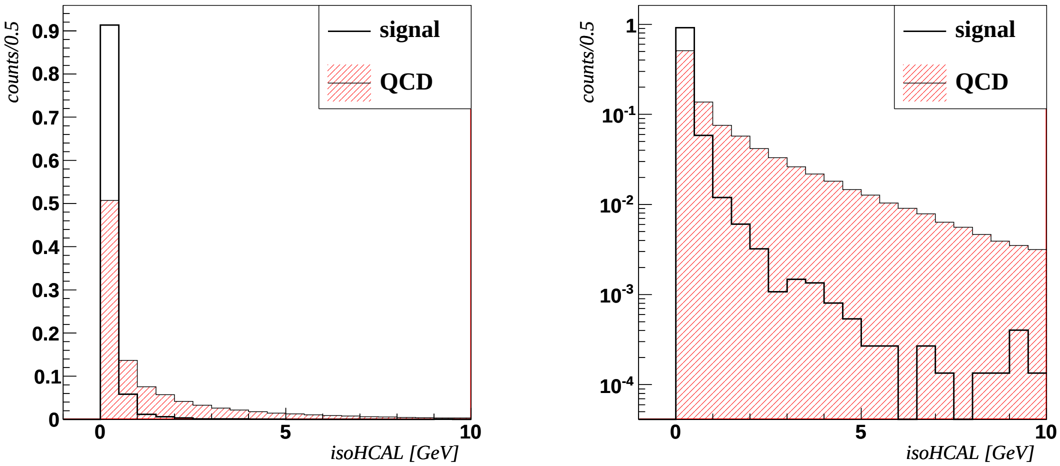

(c) HCAL isolation (d) HCAL isolation

Figure 4.10: *Isolation variables diistribution for MC signal (white fill) and MC background (filled pattern) in linear (left side) and logarithmic scale (right side).*

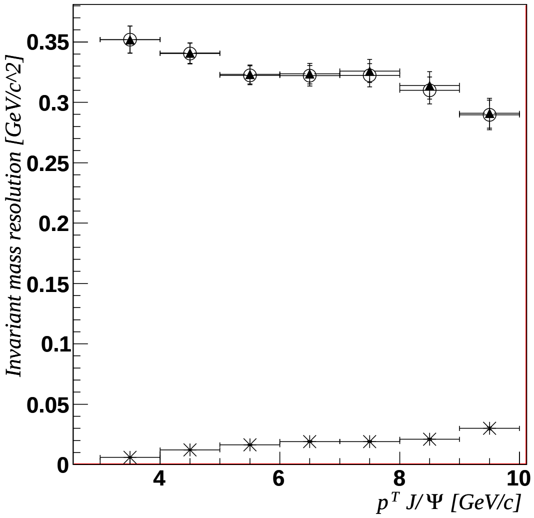

Figure 4.11: *The invariant mass resolution as a function of the J/Ψ p_T is shown with the energy and angular contribution. The resolution is defined as the Root Mean Square of the invariant mass distribution.*

4.4 Invariant Mass Resolution

The invariant mass of two electrons, in the approximation that their energy $E_e \gg m_e$, is

$$m_{J/\Psi} = \sqrt{2 \cdot E_1 E_2 (1 - cos\alpha)} \tag{4.1}$$

where $E_{1,2}$ is the energy of the 1-st and 2-nd electron and α is the angle formed by the two electrons.

An unstable particle presents an experimental invariant mass distribution represented by the convolution of two distributions: a Breit-Wigner distribution due to the finite lifetime of the particle and a distribution due to the experimental resolution. The former is characterized by an intrinsic width (Γ) proportional to $\frac{1}{\tau}$ where τ is it is mean lifetime. The J/Ψ is a very narrow resonance ($\Gamma = 79$ keV), thus the width of the invariant mass distribution is completely dominated by the experimental resolution. This depends on the energy and the angular resolutions. In order to show the different contributions of the two terms, we estimated the invariant mass resolution as the Root Mean Square (RMS) of the distribution. The invariant mass was calculated using:

∗ the MC truth energy of the electrons (E gen) and the recontructed angle between the electron directions (angle reco),

○ the reconstructed energy (E reco) and the MC truth angle (angle gen),

▲ the reconstructed energy (E reco) and angle (angle reco)

In Fig. 4.11 the invariant mass resolution is shown as a function of the transverse momentum. It results dominated by the energy resolution.

4.5 Selection cut optimization

In this section we describe the optimization of the selection cuts which will be used to enhance the statistical power of the signal.

4.5.1 General considerations

There are several ways to choose selection cut values: choosing a set of cuts for a given selection efficiency or purity or, as adopted in this work, maximizing a defined merit factor.

An unbiased procedure requires to optimize selection cuts on MC samples performing a "blind" analysis and then to look at the data with the chosen optimized selection.

For an optimization study we need both large statistics and good data representing MC samples. Unfortunately, none of the MC samples (especially the background one) fulfills these requirements.

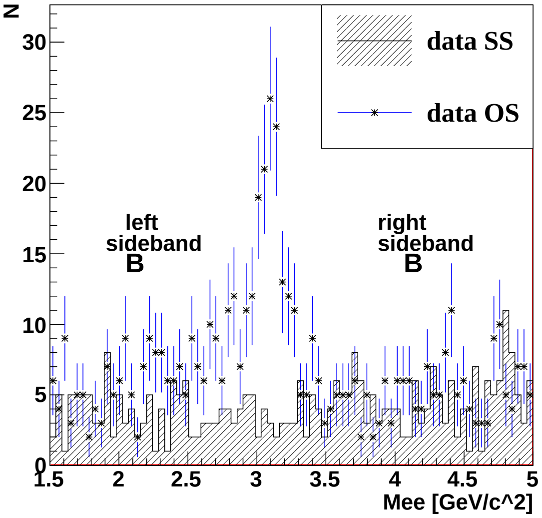

Figure 4.12: *Invariant mass distribution of same sign and opposite sign data.*

In fact, we found differences between MC simulations (for the signal) and data variable distributions expecially in isolation variables. For these reasons we have not done a blind optimization using MC, but we always used data. Doing this, we have to assure we do not introduce any bias enhancing a statistical fluctuation of the background instead of a real signal yield.

The main possible bias induced is the background shape modification in the peak region. The criteria that we optimized are not related to the charge of the single electron, so shapes of same sign and opposite sign background events are expected to be the same. Assuming that the charge misidentification at these energies is very low, same-sign sample is almost signal-free. The selection cut observables chosen for the optimization are not correlated to the invariant mass distribution so we do not expect that selection cut values can raise the background in the peak region. This is confirmed by the comparison of the invariant mass distribution of the same sign and opposite sign events showed in Fig. 4.12. In fact, in the sideband region (external to the peak region) the distributions of same sign and opposite sign events are in a good agreement and we could expect, for the above considerations, that this is true also in the peak region.

The optimization was performed on the HLT_DoublePhoton4 dataset (73 nb^{-1}).

4.5.2 The optimization procedure

We define "optimal" selection cut values those that maximize the statistical significance: $\frac{s}{\sqrt{s+b}}$ where s and b are, respectively, the signal and the background yield in the invariant mass peak region.

In the following we describe the estimation of the signal and background yields. We estimate the background extrapolating the number of events from the sidebands to the peak region. We estimate the signal yield as the number of events in the peak region minus the extrapolated background events.

We find that the same-sign invariant mass distribution is flat in a wide range ($1.5 - 5$ GeV) and we define a peak region in the range ±600 MeV around the peak estimated by the signal MC sample in order to have free signal sidebands for the background estimation. We estimate the number of background events in the peak region (N_b) as:

$$N_b = \frac{N_{side}}{side\,range} \cdot peak\,range = \frac{N_{side}}{2.3\ \text{GeV}} \cdot 1.2\ \text{GeV}$$

and the number of signal in the peak region (N_s) as:

$$N_s = N_{peak} - N_b$$

The optimization is multidimensional, varying all the selection cut values in a reasonable range In Tab. 4.5 the list of variables optimized with the variation range, the step and the optimal value found are reported.

Fig. 4.13 shows the the statistical significance as a function of the E/p cut. The graphs are reasonably smooth, to rely on the optimization process.

Selection cut	range	variation step	optimal cut
E/p	0.82 - 0.92	0.01	> 0.88
$\Delta\eta$	0.005 - 0.0095	0.0005	< 0.009
$\sigma_{\eta\eta}$	0.015 - 0.020	0.0005	< 0.016
MVA	-0.4 - 0.6	0.1	> 0.1
isoTk	0.5 - 4	0.5	< 3.5
isoECAL	1 - 10	1	< 4
isoHCAL	1 - 4	1	< 2

Table 4.5: *Summary table of the optimized cuts with variation range and variation step.*

The cut efficiencies of the optimized selection were estimated from the signal_2 MC sample. The selection efficiency at one step was computed as the number of electron pairs passing the step divided by the number of electron pairs at the previous step. They are reported in Tab. 4.6.

selection step	efficiency
electron pairs with $p_T > 4$ GeV/c	88%
electrons oppositely charged	94%
electron identification selection	71%
isolation selection	73%

Table 4.6: *Selection efficiencies estimated using the signal_2 MC sample. The efficiencies are calculated as the number of electron pairs passing the selection creteria respect to the previous step.*

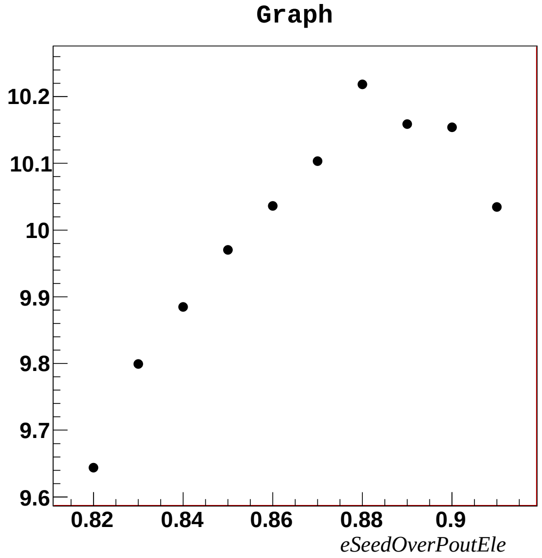

Figure 4.13: *Statistical significance as a function of the E/p cut.*

4.6 The Signal Extraction

4.6.1 The unbinned extended maximum likelihood fit

In a χ^2 minimization fitting the uncertainties in the data are expected to be normally distributed, but this is not the case for low statistics. Thus, an unbinned maximum likelihood fit was preferred [43].

The fit was used to extract the signal yield from the invariant mass distribution and the J/Ψ peak position.

We define the extended likelihood function as:

$$L(\Theta, N) = \frac{(N')^N e^{-N'}}{N!} \prod_{i=1}^{N} f(x_i|\Theta, N') \tag{4.2}$$

where N is the number of indipendent measurement of the x variable (the invariant mass), x_i is its value at the ith measurement and f is the probability density function (pdf) depending on a set of parameters that we condense in the vector Θ. In this case, the total pdf has two contributions, one from the signal pdf and one from the background pdf:

$$f(x|\Theta, N) = \frac{N_{sig} \cdot f_s(x|\Theta) + N_{bkg} f_b(x|\Theta)}{N'} \tag{4.3}$$

where N_{sig} and N_{bkg} are the expected number of signal and background events respectively. The normalization of the total *pdf* is taken into account by the poissonian term in front of the productorial where N' represents the expected total number of events.

The set of parameters $\bar{\Theta}$ that maximizes the likelihood function are estimators of the unknown real parameters Θ we are looking for with this fit.

In our case, Θ consist of the three parameters N_{sig}, N_{bkg} and m (the position of the peak of the J/Ψ invariant mass distribution).

4.6.2 Signal and background shapes

In order to correctly describe the signal invariant mass shape, in particular the tails in the distribution caused by the mis-recontruction of the energy of the electrons due to possible leakage in the calorimeter or to the large bremsstrahlung emission in the tracker material, we modelled it with an asymmetric gaussian with asymmetric exponential tails:

$$f_s(x-m) = N_{sig} \times exp\left[-\frac{(x-m)^2}{2\sigma^2_{L,R} + \alpha_{L,R}(x-m)^2}\right] \tag{4.4}$$

where N_{sig} is the signal yield, m is the peak position, σ_L and α_L correspond to the resolution and tail parameters of the distribution for $x-m<0$ and σ_R and α_R otherwise.

The signal shape α and σ parameters are taken from MC with a fit in the signal-only hypothesis. The background shape was modelled by a second order polynomial.

The signal shape is fixed to the MC in order to reduce the number of *pdf*s degree of freedom in the data fit; the background shape parameters are left as free parameters as the the J/Ψ peak position, the signal and background yields (N_{sig} and N_{bkg}).

4.7 Signal_2 MC validation

In order to use the signal_2 MC sample in the cross section measurement for the trigger and the electron reconstruction efficiencies, we checked if its requirements at generator level could be compatible with our selection. We used the signal_1 as a check sample comparing the rapidity and p_T distributions after the selection of the two samples.

The J/Ψ rapidity and the p_T distributions before selection for the signal_1 sample are shown in Fig. 4.14. The rapidity was calculated from the selected electrons without the

HLT request because the signal_1 sample was simulated only with the old J/Ψ trigger (DoublePhoton4). The J/Ψ rapidity and p_T distributions after selection for the two MC samples are compared in Fig. 4.15 and Fig. 4.16. According to the sample_1 rapidity distribution, there are no selected events with J/Ψ rapidity $|y| > 1.4$. Because of the p_T cut of our selection ($p_T > 4$ GeV), the J/Ψ p_T distribution calculated from the selected electrons shows a cut off at 8 GeV. The signal_2 is therefore a representative J/Ψ sample.

In the following analysis the only MC sample used is signal_2.

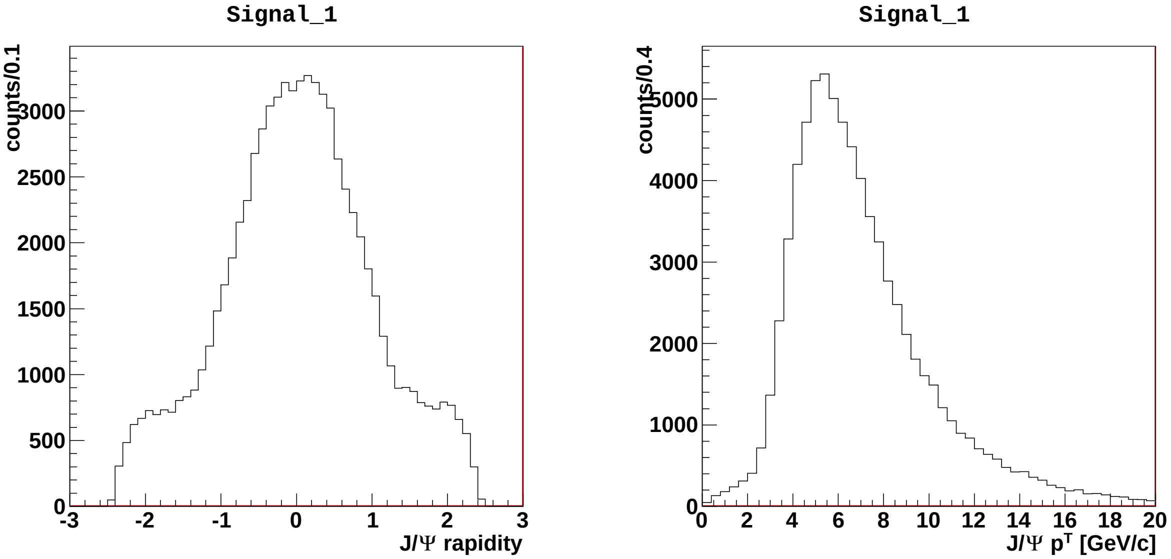

(a) signal_1 rapidity

(b) signal_1 p_T

Figure 4.14: *J/Ψ rapidity and transverse momentum calculated from the electrons of signal_1 before the selection procedure.*

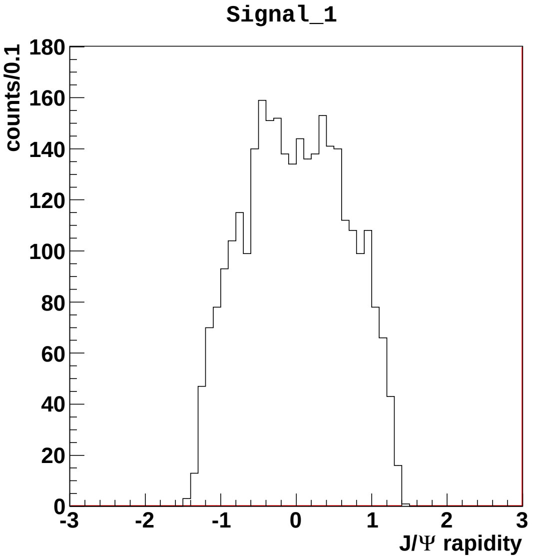

(a) signal_1

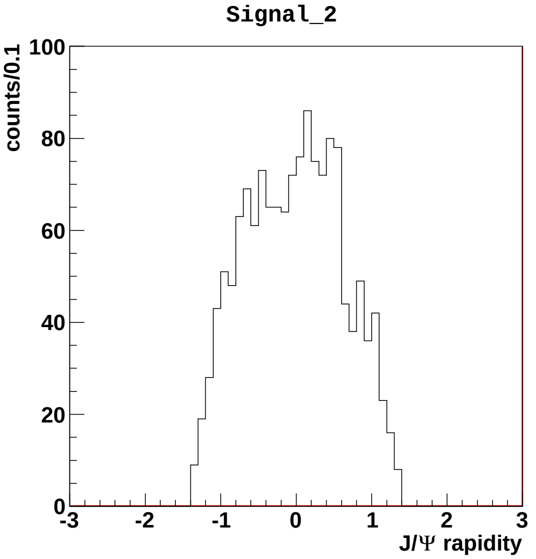

(b) signal_2

Figure 4.15: *J/Ψ rapidity calculated from the selected electrons of signal_1 (on the left) and signal_2 (on the right).*

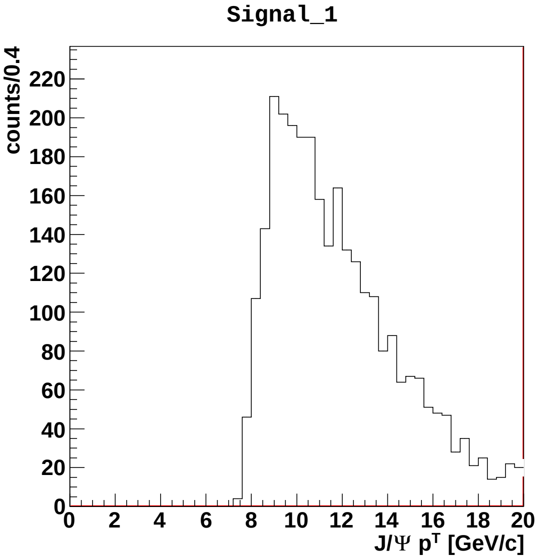

(a) signal_1

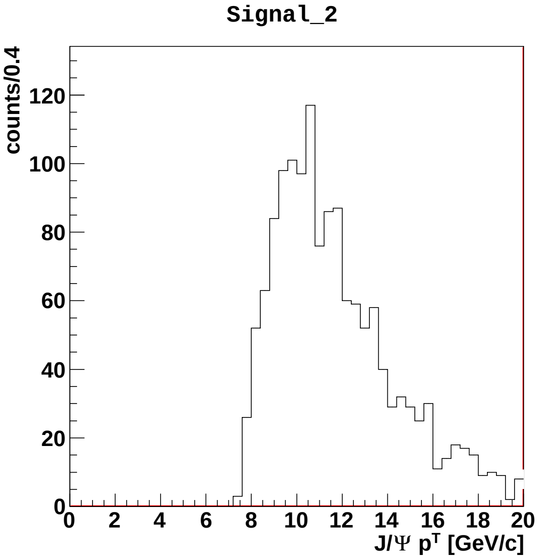

(b) signal_2

Figure 4.16: *J/Ψ transverse momentum calculated from the selected electrons of signal_1 (on the left) and signal_2 (on the right).*

4.8 Selection result

Fig. 4.17 shows the invariant mass distribution obtained using the optimized selection and fitted as described in previous paragraph. The plot on top (Fig. 4.17(a)) is the fitted invariant mass distribution of the signal MC distribution; the one on bottom (Fig. 4.17(b)) is the data invariant mass distribution. The J/Ψ yield estimated by a data integrated lumosity of 1.8 pb^{-1} in the barrel region is 1257 ± 41.

The fit parameters are reported in Tab. 4.7.

Signal shape (MC) fit		
	value	statistical uncertainty
σ_L[GeV]	0.066971	0.0047
σ_R[GeV]	0.0401	0.0029
α_L	0.206	0.010
α_R	0.1567	0.0058
Data fit		
	value	statistical uncertainty
N_{sig}	1257	41
N_{bkg}	959	39
m[GeV]	3.0977	0.0023

Table 4.7: *The table shows the signal and background fit parameters given by the unbinned maximum likelihood fit. The signal shape parameter are evaluated fitting the signal MC invariant mass distribution. The background shape parameters, the yields and the signal peak position are left floating in the data fit.*

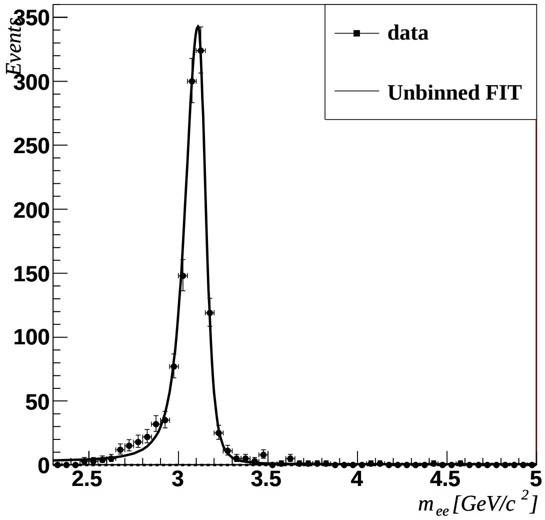

(a) signal MC

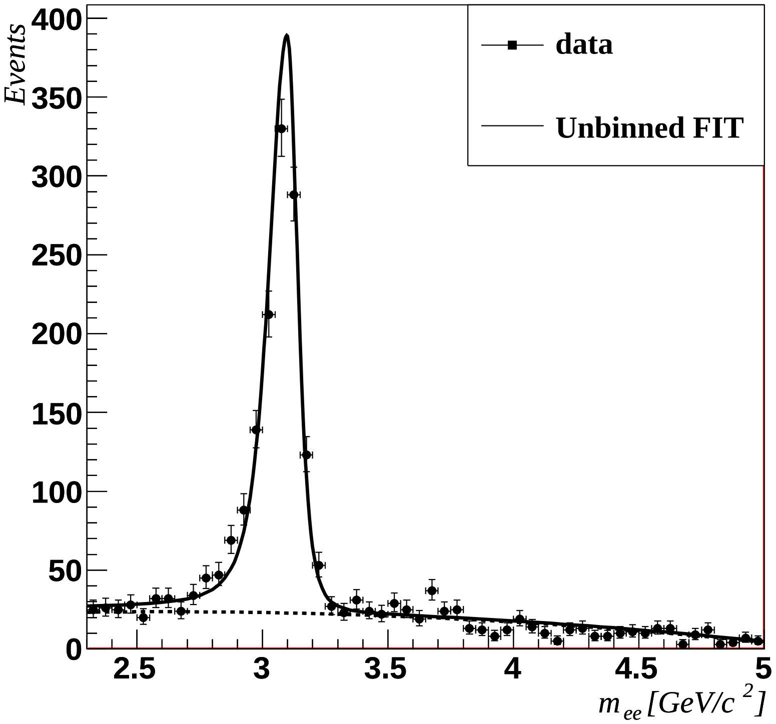

(b) data

Figure 4.17: *Invariant mass distribution of the selected electron pairs showing the* J/Ψ *peak with* 1.8 pb^{-1}*. The* J/Ψ *yield, given by the unbinned maximum likelihood fit, is* 1257 J/Ψ*s. The signal shape was modelled on the* MC *sample and is well described by a Cruijff function; for the background a second order polynomial function was used.*

Chapter 5

Study of low p_T electrons

As already pointed out, the reconstruction of low p_T electrons is a challenging task, but it could be crucial in the discovery of the Higgs boson. In fact, for the Higgs discovery, one of the most important physics channels is $H \rightarrow ZZ^* \rightarrow 4\ell$. The p_T distribution of the four electrons of a low mass Higgs boson is shown in Fig. 5.1. The lowest p_T electron presents a transverse momentum distribution peaked in the very low transverse momentum region, the same of the J/Ψ electrons. Thus, a good reconstruction efficiency of low p_T electrons becomes crucial and the J/Ψ channel a very useful test. In this chapter we will measure the electron reconstruction and selection efficiencies and we will show the comparison between data and MC of the selection variables.

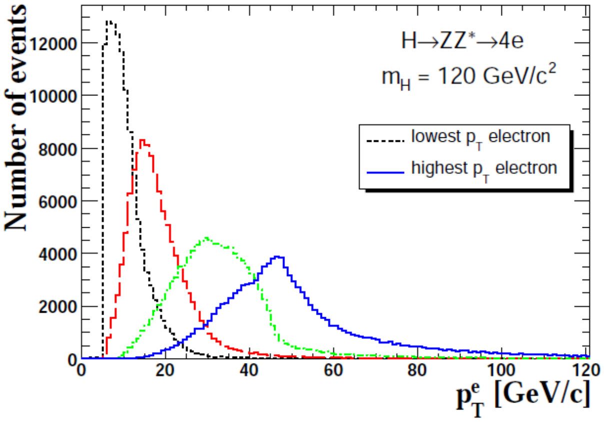

Figure 5.1: *Transverse momentum distributions of the four electrons of the* $H \rightarrow ZZ^* \rightarrow 4\ell$ *decay channel.*

5.1 Electron selection efficiency

We used the Tag&Probe (T&P) method to measure the efficiency of the optimized electron selection directly on data.

The aim of a T&P is to produce a pure electron sample using a di-electron resonance. The method consists of requiring very tight criteria on one of the two electrons (named "tag") and using the other one (named "probe") to study its properties.

Since both the J/Ψ yield and the selection efficiency will be used for the cross section measurement, we used two indipendent datasets: 0.6 pb^{-1} were used for the signal yield measurement and the remaining 1.2 pb^{-1} for the efficiency measurement. Since the square value of electron efficiency is used in the cross section measurement, we used a double statistics sample for this measurement respect to the yield one. In such a way the statistical errors are expected to be of the same order of magnitude.

The tag is defined as an electron satisfying the optimized selection criteria described in the previous chapter. The probe is an electron required to have:

- $p_T > 4$ GeV/c
- opposite charge with respect to the tag electron

We define the "denominator sample" as the set of all the T&P pairs and the "numerator sample" as the set of T&P pairs in which the probe electron satisfy our selection criteria.

The single electron selection efficiency ϵ_{sel} is thus the ratio between the signal yield of the numerator (N_{sig}^{sel}) and the denominator (N_{sig}^{tot}) samples:

$$\epsilon_{sel} = \frac{N_{sig}^{sel}}{N_{sig}^{tot}} \pm \frac{N_{sig}^{sel}}{N_{sig}^{tot}} \sqrt{\frac{err(N_{sig}^{sel})}{N_{sig}^{sel}} \oplus \frac{err(N_{sig}^{tot})}{N_{sig}^{tot}}} \tag{5.1}$$

where the signal yields are extracted with the unbinned fit following the procedure described in Sec. 4.6. $err(N_{sig}^{sel})$ and $err(N_{sig}^{tot})$ are the numerator and denominator sample yield errors given by the fit.

The fitted invariant mass distributions for the numerator and denominator sample are shown in Fig. 5.2(a) and Fig. 5.2(b) respectively.

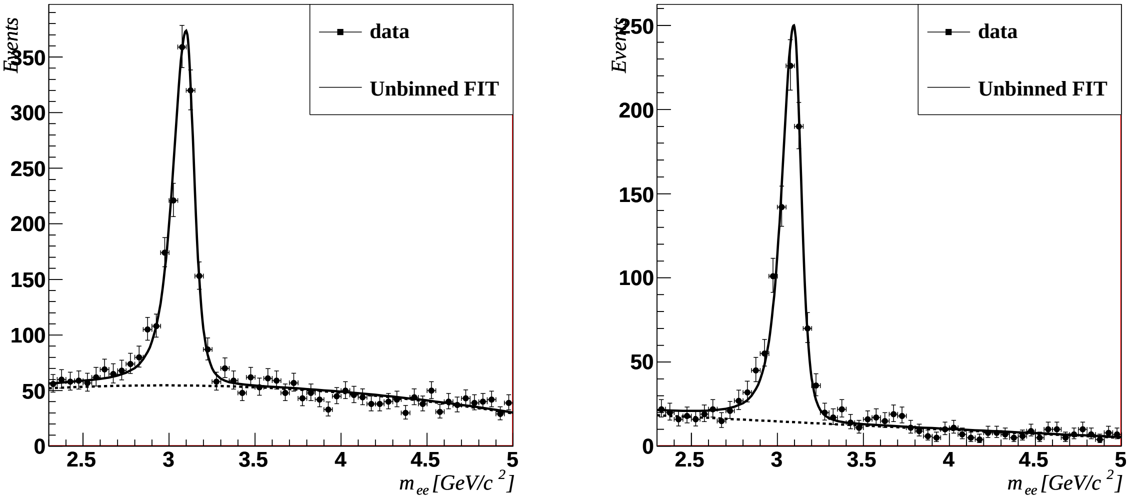

(a) (b)

Figure 5.2: *The plots show the invariant mass distribution for electron - electron T&P pair for the denominator sample (on the left) and for the numerator sample (on the right). The "denominator sample" is defined as the set of all the T&P pairs and the "numerator sample" as the set of T&P pairs in which the probe electron satisfy the selection criteria. The signal shape parameter are evaluated fitting the signal MC invariant mass distribution. The background shape parameters, the yields and the signal peak position are left floating in the data fit.*

(a) denominator sample

Fit signal shape		
	value	stat uncertainty
m [GeV]	3.1066	0.0081
σ_L [GeV]	0.07071	0.00079
σ_R [GeV]	0.0439	0.0058
α_L	0.2191	0.0078
α_R	0.1637	0.0057
N_{sig}	1522	39
Data fit		
	value	stat uncertainty
N_{sig}	1220	46
N_{bkg}	2601	59
m [GeV]	3.0993	0.0028

(b) numerator sample

Fit signal shape		
	value	stat uncertainty
m [GeV]	3.1098	0.0043
σ_L [GeV]	0.0658	0.0045
σ_R [GeV]	0.0402	0.0029
α_L	0.216	0.010
α_R	0.1583	0.0057
N_{sig}	1205	35
Data fit		
	value	stat uncertainty
N_{sig}	821	34
N_{bkg}	625	31
m [GeV]	3.0962	0.0030

Table 5.1: *The left table shows the fit parameters of the denominator sample, the one on the right side shows the fit parameters of the numerator sample. The signal shape parameters are evaluated fitting the signal MC invariant mass distribution. The background shape parameters, the yields and the signal peak position are left floating in the data fit.*

We report in Tab. 5.1 the fit results. The single electron selection efficiency is

$$\epsilon_{sel} = 67.3\% \pm 3.7\%$$

the efficiency estimated on the MC sample is $\epsilon_{sel} = 79.2\% \pm 2.6\%$.

The difference between data and MC is almost due to the different isolation variable distributions as will be shown in the next section.

The efficiency estimated by the T&P method on the MC sample results 7% larger than the efficiency estimated in the previous Chapter in Tab. 4.6. This can be due to the fact that the selection efficiency is not completely indipendent on the request of the tag electron.

5.2 Electron identification commissioning

In this section we will present the comparison of the J/Ψ electron distributions between data and MC in order to investigate the differences between them and validate the MC simulation for low p_T electrons.

The T&P method illustrated in the previous section provides an electron sample not biased by our selection criteria, but it is still background contaminated. Hence, we divided the sample into a peak region defined in a ±100 MeV range around the J/Ψ mass and a sideband region in the range $3.5 \div 5$ GeV/c^2 (signal-free). Such a small peak region is a compromise between the need of statistics and the need to keep the background contamination low. The sideband probe electron distribution was normalized to the expected number of background events in the peak region (N_{bkg}^{peak}) as given by the fit to the invariant mass distribution performed in the previous section:

$$N_{bkg}^{peak} = 275 \quad N_{bkg}^{side} = 1293$$

Thus, we subtracted the variable distribution of the signal-free probe electron sample (sideband) from the signal (peak) distribution. The obtained variable distribution is representative of a pure signal sample.

Fig. 5.3 and Fig. 5.4 show the electron identification variable distributions used in our selection for the signal_2 MC sample and data. The electron isolation variables are shown in Fig. 5.5. Fig. 5.6. There is a good agreement between data and MC in the electron identification variables. The disagreement in the isolation variables is probably do to the pile-up that is not simulated. The same behaviour was experienced in W analysis, the study is in progress.

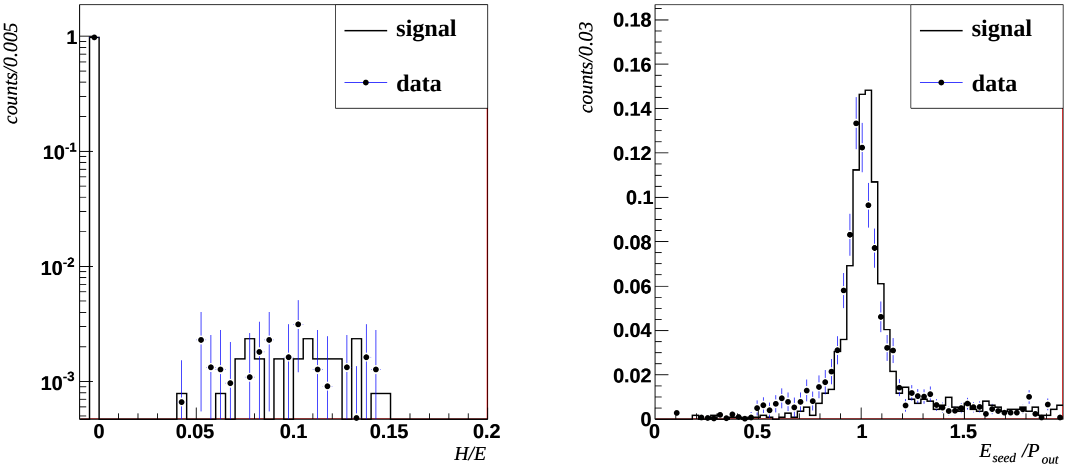

(a) H/E (b) E/p

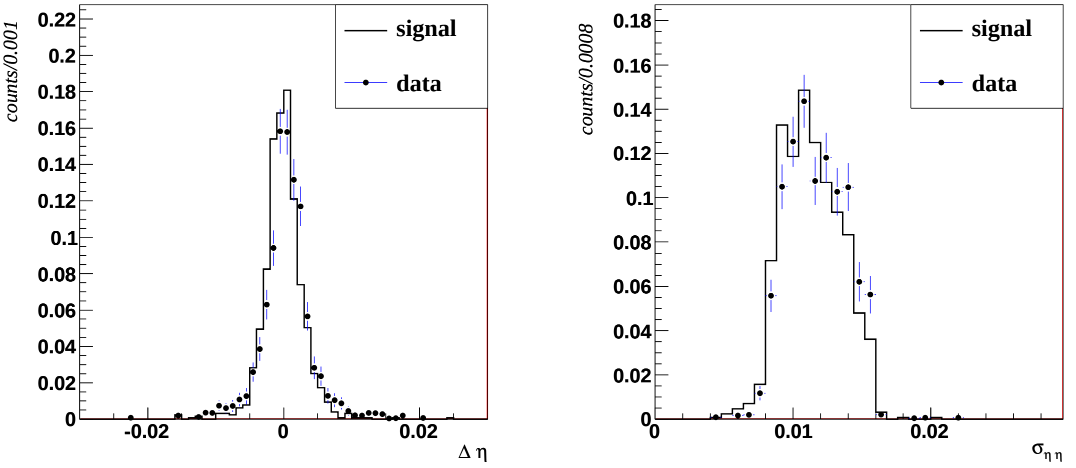

(c) $\Delta\eta$ (d) $\sigma_{\eta\eta}$

Figure 5.3: *Electron identification variable distributions for MC (histograms) and data (points). The distributions are obtained by a T&P procedure.*

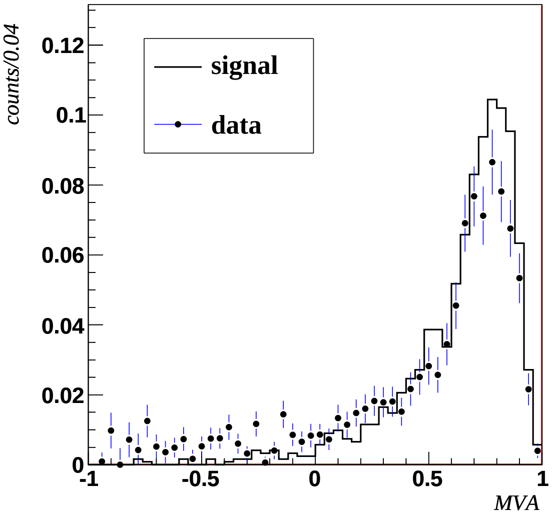

Figure 5.4: *MVA variable distributions for TrackerDriven and EcalDriven electrons for* MC *(histograms) and data (points). The distributions are obtained by a* T&P *procedure.*

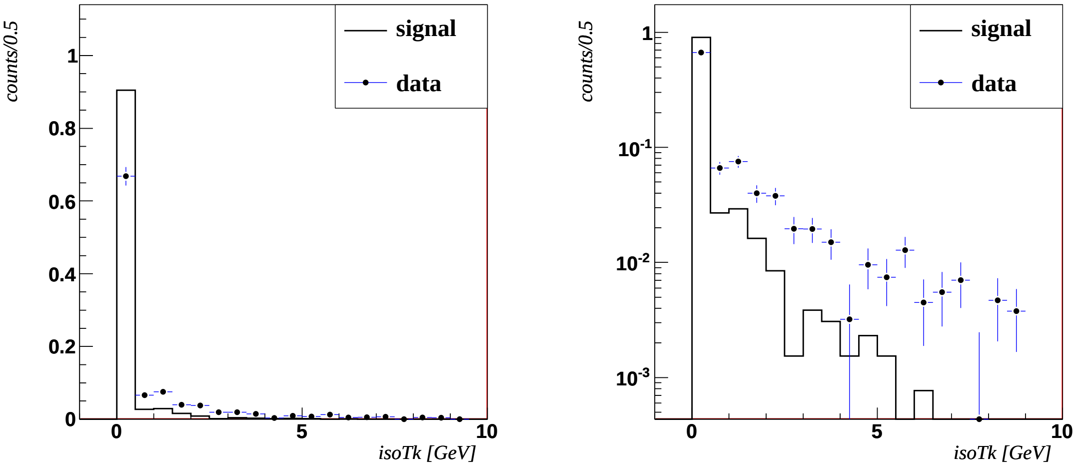

(a) isoTk

(b) isoTk log

Figure 5.5: *isoTk isolation variable distributions for* MC *(histograms) and data (points) in linear scale (left) and logscale (right). The distributions are obtained by a* T&P *procedure.*

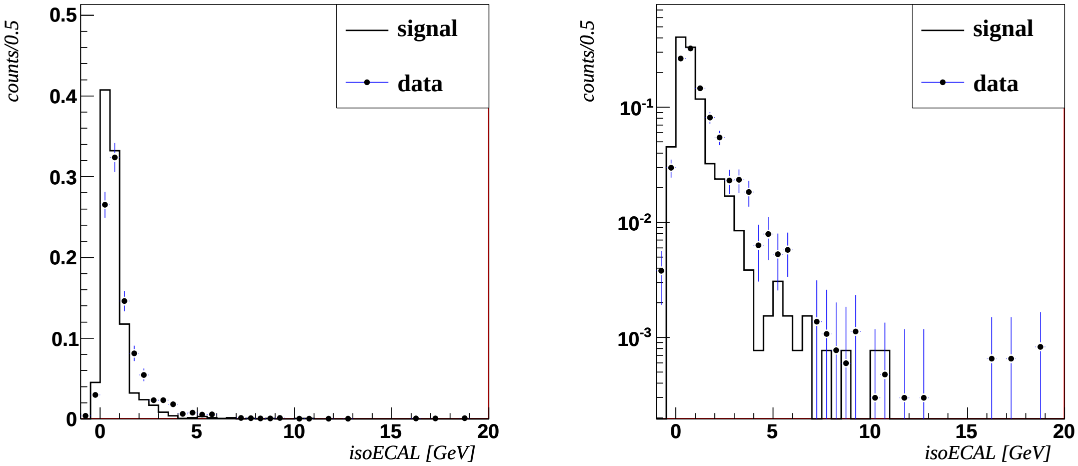

(a) isoECAL (b) isoECAL log

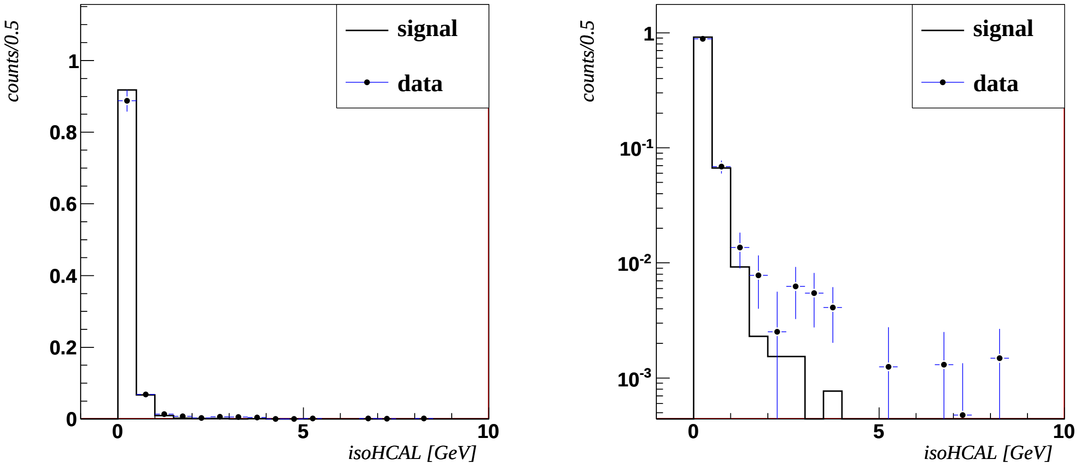

(c) isoHCAL (d) isoHCAL log

Figure 5.6: *isoECAL and isoHCAL isolation variable distributions for* MC *(histograms) and data (points) in linear scale (left) and logscale (right). The distributions are obtained by a* T&P *procedure.*

5.3 ECAL absolute scale calibration with the J/Ψ peak

The J/Ψ can be also used to check the absolute scale of ECAL.

The ECAL energy scale factor G is the conversion factor between the ADC counts registered by the electronics and the corresponding energy value (GeV). It was measured at the test beam using a 5×5 crystal matrix[1].

Since no scale factor is used in the MC simulation where all the hits are directly expressed in energy units, the energy scale factor can be checked by the comparison between the J/Ψ peak position in data and MC. If we consider G_{true} the correct scale factor, we can define $g = \frac{G}{G_{true}}$. The electron energy will be $E = E_{true} \cdot g$ and consequently the J/Ψ invariant mass peak will be found shifted of a factor g:

$$m_{data} = \sqrt{2 \cdot gE_1 \cdot gE_2 \cdot (1 - cos(\alpha))} = g \cdot m_{J/\Psi}$$

The relative correction of the absolute scale is estimated by the relative shift of the peak position $\frac{\Delta m}{m_{J/\Psi}} = \frac{m_{data} - m_{\mathrm{MC}}}{m_{J/\Psi}} = g - 1$

For this measurement, we have used the whole statistics available at the moment of writing, 1.8 pb^{-1} (see Tab. 4.3).

5.3.1 Measurement procedure

We used the optimized selection procedure described in the previous chapter. The invariant mass of the selected J/Ψ electrons was computed using the direction estimated by the track extrapolated at the vertex and the corrected energy estimated by the SC (E_{SC}).

The peak position (m) was estimated by the unbinned maximum likelihood described in Sec. 4.6. The fit of the MC invariant mass distribution was performed in the signal-only hypothesis leaving all the fit function parameters free. The number of degree of freedom of the pdfs was reduced for the fit of the invariant mass distribution in the data. The signal shape parameters were fixed at the MC fit values; the background shape parameters, the peak position and signal and background normalizations are free parameters of the fit.

---

[1] The motivation of this cluster size was already mentioned in Sec. 3.1.2.

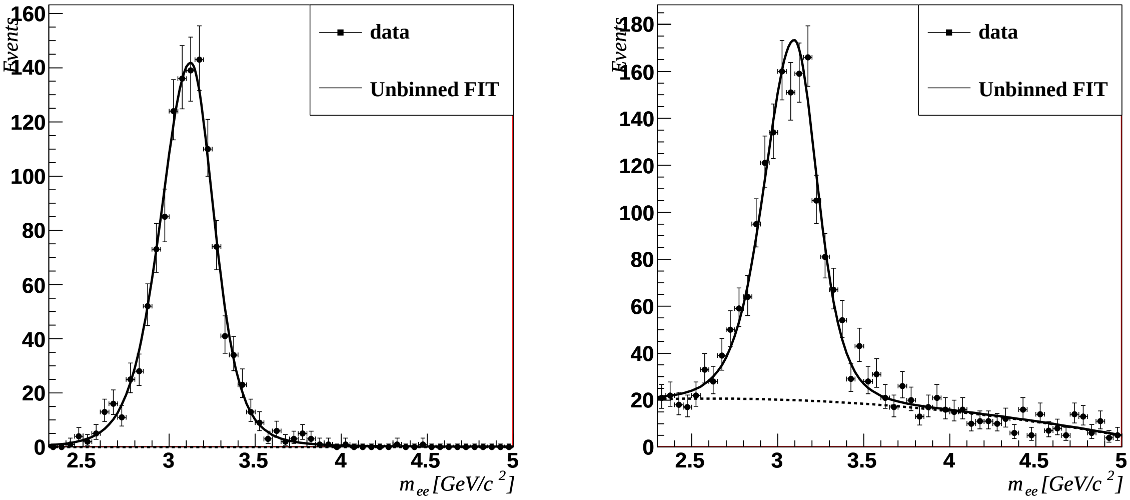

(a) MC sample (b) data opposite sign

Figure 5.7: *Invariant mass distribution for MC (on the left) and for data (on the right) calculated using the direction estimated by the track at the vertex and the corrected energy of the SC associated to the electrons. In the data fit, the signal shape parameter are fixed at the MC fit values. The background shape parameters, the yields (N_{sig}, N_{bkg}) and the peak position (m) are left floating in the data fit.*

In Fig. 5.7 are shown the invariant mass distribution of signal MC on the left and of data on the right side. The unbinned fit is superimposed as a continuos line. The fit parameters are shown in Tab. 5.2.

The peak position from the signal MC fit is:

$$m_{MC} = 3.130 \pm 0.014 \text{ GeV}$$

and the J/Ψ peak measured from data is:

$$m_{data} = 3.102 \pm 0.006 \text{ GeV}$$

The relative correction factor is estimated by the peak position shift between MC and data as:

$$\frac{\Delta m}{m} = \frac{m_{data} - m_{\rm MC}}{m_{J/\Psi}} \tag{5.2}$$

Fit signal shape		
	value	statistical uncertainty
m [GeV]	3.130	0.014
N_{sig}	1197	34
σ_L [GeV]	0.179	0.013
σ_R [GeV]	0.128	0.010
α_L	0.095	0.022
α_R	0.140	0.012

Data fit		
	value	statistical uncertainty
m [GeV]	3.102	0.006
N_{sig}	1319	45
N_{bkg}	897	40

Table 5.2: *Invariant mass fit parameters. The values of σ_L and σ_R result larger than the those obtained using the combination of the track-momentum and ECAL energy for the electron energy estimation. The energy resolution of the combined method provides a narrower peak (the width of the J/Ψ is due only to the experimental resolution).*

where $m_{J/\Psi}$ is the J/Ψ mass given by the Particle Data Group (PDG) and reported in Sec. 1.1.

The statistical uncertainty is:

$$err\left(\frac{\Delta m}{m}\right) = \frac{\sqrt{err(m_{\mathrm{MC}}) \oplus err(m_{data})}}{m_{J/\Psi}} \tag{5.3}$$

The relative absolute scale correction is $-0.89\% \pm 0.49\%\,(stat)$, in agreement with the π^0 measurement [44]: $\frac{\Delta m_{\pi^0}}{m_{\pi^0}} = -0.7\% \pm 0.02\%\,(stat) \pm 0.9\%\,(syst)$ in ECAL barrel.

5.4 J/Ψ cross section measurement

The cross section for prompt J/Ψ production with rapidity $\left|y^{J/\Psi}\right| < 1.4$ and $p_T > 4$ GeV/c is defined as:

$$\sigma(J/\Psi \to e^+e^-) = \frac{N_{sig}}{\mathcal{L} \cdot \epsilon} \tag{5.4}$$

where N_{sig} is the number of J/Ψ events in the ECAL barrel measured in $\mathcal{L}$ integrated luminosity of data and ϵ is the total efficiency.

The cross section measurement error is thus given by

$$err(\sigma) = \frac{N_{sig}}{\mathcal{L} \cdot \epsilon} \sqrt{\frac{err(N_{sig})}{N_{sig}} \oplus \frac{err(\mathcal{L})}{\mathcal{L}} \oplus \frac{err(\epsilon)}{\epsilon}} \tag{5.5}$$

In Sec. 4.8 we have described the signal yield (N_{sig}) extraction procedure. N_{sig} will be measured in the next section for an integrated luminosity of 0.6 pb^{-1}. The luminosity is known with an uncertainty of 11% [45]. This error is expected to be reduced at 5% at the end of this year.

As far as the the global efficiency (ϵ), we have factorized it into three main parts:

$$\epsilon = \epsilon_{\mathrm{HLT}} \cdot \epsilon_{RECO|\mathrm{HLT}} \cdot (\epsilon_{sel|RECO})^2 \tag{5.6}$$

where ϵ_{HLT} is the trigger efficiency, $\epsilon_{RECO|\mathrm{HLT}}$ is the electron reconstruction efficiency given the trigger and $\epsilon_{sel|RECO}$ is the single electron selection efficiency given a reconstructed electron.

5.4.1 Signal yield

The J/Ψ yield measured by the procedure described in Sec. 4.6 on a data integrated lumosity of 0.6 pb^{-1} in the barrel region is 389 ± 23. The invariant mass distribution is shown Fig. 5.8.

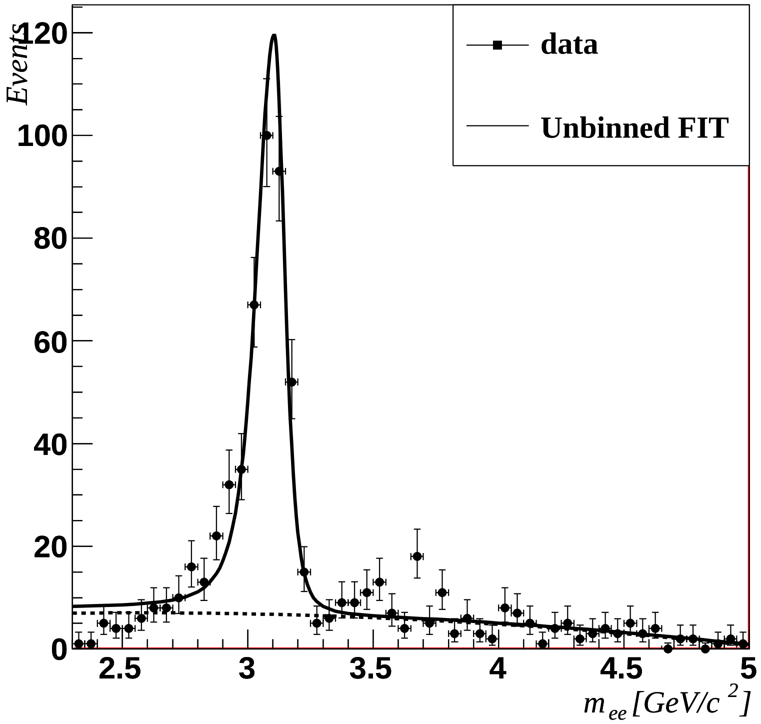

Figure 5.8: *Invariant mass distribution of the selected electron pairs showing the* J/Ψ *peak with* 0.6 pb^{-1}. *The* J/Ψ *yield, given by the unbinned maximum likelihood fit, is* 389 ± 23 J/Ψ*s. The signal shape was modelled on the* MC *sample and is well described by a Cruijff function; for the background a second order polynomial function was used.*

5.4.2 Efficiencies

Trigger efficiency

As already pointed out in Sec. 4.3.3 the J/Ψ dedicated triggers are the unprescaled triggers with the lowest p_T request. At the moment of writing, there were no indipendent triggers that could be used to measure the J/Ψ trigger efficiency on data. Thus, we have estimated the trigger efficiency from the signal_2 MC sample.

We defined the trigger efficiency ϵ_{HLT} as the ratio between the number of J/Ψ events firing the trigger and the number of events in the MC sample passing the MC event filter of signal_2.

The trigger efficiency term is thus estimated as:

$$\epsilon_{\text{HLT}} = \frac{N_{\text{HLT}}}{N_{\text{MC}}} = \frac{4418}{235603} = 1.875 \cdot 10^{-2} \tag{5.7}$$

and the statistical uncertainty is given by:

$$err(\epsilon_{\text{HLT}}) = \sqrt{\frac{\epsilon_{\text{HLT}} \cdot (1 - \epsilon_{\text{HLT}})}{N_{\text{MC}}}} = 2.8 \cdot 10^{-4} \tag{5.8}$$

The trigger efficiency is then $1.875\% \pm 0.028\%$.

Electron reconstruction efficiency

The electron recontruction efficiency $\epsilon_{RECO|\text{HLT}}$ was evaluated from the MC simulation as:

$$\epsilon_{RECO} = \frac{N_{2ele}^{barrel}}{N_{\text{HLT}}} = \frac{2854}{4418} = 0.646 \tag{5.9}$$

where N_{2ele}^{barrel} is the number of events firing the trigger path with at least 2 reconstructed electrons in the barrel.

The statistical uncertainty is given by:

$$err(\epsilon_{RECO}) = \sqrt{\frac{\epsilon_{RECO} \cdot (1 - \epsilon_{RECO})}{N_{\text{HLT}}}} = 7.2 \cdot 10^{-3} \tag{5.10}$$

The efficiency of reconstructing two electrons in ECAL barrel in events firing the HLT path is $64.60\% \pm 0.72\%$.

Global efficiency

The electron selection efficiency was measured in Sec. 5.1: $\epsilon_{sel} = 67.3\% \pm 3.7\%$

The global efficiency ϵ is then:

$$\epsilon = 0.549\% \pm 0.036\% \tag{5.11}$$

5.5 $J/\Psi \rightarrow e^+e^-$ cross section

The cross section of un-polarized prompt J/Ψ production decaying into electrons in the barrel region ($|\eta| < 1.479$) is measured in 0.6 pb^{-1} with a 9% of statistical uncertainty and 11% of uncertainty on the luminosity measurement:

$$\sigma(J/\Psi \rightarrow e^+e^-) = (122 \pm 11\,(stat) \pm 13\,(lumi))\ \text{nb} \tag{5.12}$$

This value is in agreement with the statistically more accurate measurement performed by the CMS experiment in the muonic decay channel (132.2 nb) with 100 nb^{-1} of integrated luminosity and presented in [46].

Conclusions

The Large Hadron Collider (LHC) started to collide proton beams at the center of mass energy of 7 TeV in April 2010. In this work we have analyzed the first 1.8 pb^{-1} of data collected until the end of August by the Compact Muon Solenoid (CMS) experiment studying the J/Ψ events decaying into an electron positron pair ($J/\Psi \rightarrow e^+e^-$).

A J/Ψ event selection procedure, optimization and the signal extraction were developed and described in Chapter 4.

The resulting J/Ψ sample was used for the study of electrons with low transverse momentum ($p_T < 10$ GeV). The improvement in their reconstruction efficiency will be crucial in the Higgs boson hunting in the $H \rightarrow ZZ^* \rightarrow 4\ell$. This is a very clean decay channel and it is particularly suitable for a high mass Higgs boson. The lowest p_T lepton, in fact, is shown to have a transverse momentum spectrum in the low p_T region (below 10 GeV).

In Chapter 5 we have shown the comparison between data and Monte Carlo (MC) electron distributions and we found a good agreement in the electron identification variables and some discrepancies in the isolation variables, probably due to the not simulated pile-up.

The challenges of the low p_T electron reconstruction are visible in the electron reconstruction efficiency measured from data ($\epsilon_{sel} = 67.3\% \pm 3.7\%$).

The J/Ψ sample was also used in order to check the energy scale of the CMS electromagnetic calorimeter (ECAL) looking at the shift of the J/Ψ peak position between data and MC. The relative absolute scale correction is $-0.89\% \pm 0.49\% \, (stat)$. It is in agreement with recent measurements performed using the π^0. The J/Ψ will be used for the ECAL calibration together with the π^0 and the Z boson providing an intermediate point in the energy scale between them.

Finally, the cross section of prompt J/Ψ with $p_T^{J/\Psi} > 4$ GeV and rapidity $|y| < 1.4$ was measured: $\sigma(J/\Psi \rightarrow e^+e^-) = (122 \pm 11\,(stat) \pm 13\,(lumi))$ nb. It is in agreement with the measurement in the muonic decay channel. This is the first measurement of prompt J/Ψ cross section in the electronic decay channel performed in CMS.

Acknowledge

This thesis is the result of an intense work started last summer thanks to Prof. Giovanni Organtini who proposed me for the Summer Student experience at CERN and thanks to Dott. Marcella Diemoz who gave me this opportunity.

This result could not be possible without the precious guide of Riccardo Paramatti who followed carefully my work with thoughtfull and usefull comments.

I think there is no enough space to thank Emanuele Di Marco and Chiara Rovelli; there is no enough space to remind all the times they were ready to give me a hand or to look at my code (usually not clear also to me); there is no enough space to thank them to the unfailing material and spiritual support.

I am grateful to Prof. Longo to have so patiently read and re-read this thesis proposing me comments and observations.

I would like to thank all the CMS group of Rome, Francesca Cavallari and Paolo Meridiani.

Thanks to Roberta Arcidiacono for integrating my work into the “ECAL calibration with J/Ψ” group at CERN.

Last but not least, thank to all my family and people who love me anyway.

Bibliography

[1] S. Weinberg, "Conceptual foundations of the unified theory of weak and electromagnetic interactions," *Rev. Mod. Phys.*, vol. 52, pp. 515–523, Jul 1980. 1.1

[2] S. L. Glashow, "Partial-symmetries of weak interactions," *Nuclear Physics*, vol. 22, no. 4, pp. 579 – 588, 1961. 1.1

[3] S. Weinberg, "A model of leptons," *Physical Review Letters*, vol. 19, no. 21, pp. 1264–1266, 1967. 1.1

[4] A. Salam, "Elementary particle theory, ed," *N. Svartholm, Stockholm, Almquist and Wiksell*, vol. 367, 1968. 1.1

[5] P. W. Higgs, "Broken symmetries and the masses of gauge bosons," *Phys. Rev. Lett.*, vol. 13, pp. 508–509, Oct 1964. 1.1

[6] P. Higgs, "Broken symmetries, massless particlees and gauge fields," *Physics Letters*, vol. 12, no. 2, pp. 132 – 133, 1964. 1.1

[7] M. Gell-Mann, "A schematic model of baryons and mesons," *Phys. Lett*, vol. 8, no. 214-215, p. 2, 1964. 1.1

[8] M. Han and Y. Nambu, "Three-triplet model with double SU (3) symmetry," *Phys. Rev*, vol. 139, pp. B1006–B1010, 1965. 1.1

[9] H. Fritzsch, M. Gell-Mann, and H. Leutwyler, "Advantages of the color octet gluon picture, Phys. Lett," 1973. 1.1

[10] D. Gross and F. Wilczek, "Asymptotically free gauge theories. I," *Physical Review D*, vol. 8, no. 10, pp. 3633–3652, 1973. 1.1

[11] S. Weinberg, “Non-Abelian gauge theories of the strong interactions,” *Physical Review Letters*, vol. 31, no. 7, pp. 494–497, 1973. 1.1

[12] S. C. C. Ting *et al.*, “Experimental Observation of a Heavy Particle J,” *Phys. Rev. Lett.*, vol. 33, pp. 1404–1406, Dec 1974. 1.1

[13] B. Richter *et al.*, “Discovery of a Narrow Resonance in e^+e^- Annihilation,” *Phys. Rev. Lett.*, vol. 33, pp. 1406–1408, Dec 1974. 1.1

[14] K. Nakamura and P. D. Group, “Review of particle physics,” *Journal of Physics G: Nuclear and Particle Physics*, vol. 37, no. 7A, p. 075021, 2010. 1.1

[15] Z. Yang, A. C. Kraan, and f. t. C. collaboration, “Quarkonium Production Studies in CMS,” 2008. 1.3

[16] The CDF Collaboration, “Production of J/Ψ Mesons from χ_c Meson Decays in $p\bar{p}$ Collisions at $\sqrt{s} = 1.8TeV$,” *Phys. Rev. Lett.*, vol. 79, pp. 578–583, Jul 1997. 1.3

[17] N. Brambilla *et al.*, “Heavy quarkonium physics,” 2004. 1.3

[18] The CDF Collaboration, “Polarizations of J/Ψ and $\psi(2S)$ Mesons Produced in $p\bar{p}$ Collisions at $\sqrt{s} = 1.96$ TeV,” *Phys. Rev. Lett.*, vol. 99, p. 132001, Sep 2007. 1.3

[19] Brüning, Oliver Sim and Collier, Paul and Lebrun, P and Myers, Stephen and Ostojic, Ranko and Poole, John and Proudlock, Paul, *LHC Design Report.* Geneva: CERN, 2004. 2.1

[20] The CMS Collaboration, “The CMS experiment at the CERN LHC,” *Journal of Instrumentation*, vol. 3, 2008. 2.2

[21] The CMS Collaboration, *The CMS magnet project: Technical Design Report.* Technical Design Report CMS, Geneva: CERN, 1997. 2.2.2

[22] The CMS Collaboration, *The CMS tracker system project: Technical Design Report.* Technical Design Report CMS, Geneva: CERN, 1997. 2.2.3

[23] The CMS Collaboration, *The CMS tracker: addendum to the Technical Design Report.* Technical Design Report CMS, Geneva: CERN, 2000. 2.2.3

[24] *The CMS ECAL: Technical Design Report*. Technical Design Report CMS, Geneva: CERN, December 1997. 2.2.4

[25] P. Bloch, R. Brown, P. Lecoq, and H. Rykaczewski, *Changes to CMS ECAL electronics: addendum to the Technical Design Report*. Technical Design Report CMS, Geneva: CERN, 2002. 2.2.4

[26] P. Adzic *et al.*, "Energy resolution of the barrel of the cms electromagnetic calorimeter," *Journal of Instrumentation*, vol. 2, no. 04, p. P04004, 2007. 2.2.4

[27] The CMS Collaboration, *The CMS hadron calorimeter project: Technical Design Report*. Technical Design Report CMS, Geneva: CERN, 1997. 2.2.5

[28] The CMS ECAL-HCAL Collaboration, "The CMS Barrel Calorimeter Response to Particle Beams from 2 to 350 GeV/c." CMS NOTE 2008/034, June 2008. 2.2.5

[29] The CMS Collaboration, *The CMS muon project: Technical Design Report*. Technical Design Report CMS, Geneva: CERN, 1997. 2.2.6

[30] S. Baffioni, C. Charlot, F. Ferri, D. Futyan, P. Meridiani, I. Puljak, C. Rovelli, R. Salerno, and Y. Sirois, "Electron reconstruction in cms," *The European Physical Journal C - Particles and Fields*, vol. 49, pp. 1099–1116, 2007. 10.1140/epjc/s10052-006-0175-5. 3.1

[31] Frühwirth, R., "Application of kalman filtering to track and vertex fitting," *Nuclear Instruments and Methods in Physics Research Section A: Accelerators, Spectrometers, Detectors and Associated Equipment*, vol. 262, no. 2-3, pp. 444 – 450, 1987. 3.1.1

[32] Frühwirth, R., "A gaussian-mixture approximation of the bethe-heitler model ofelectron energy loss by bremsstrahlung," *Computer Physics Communications*, vol. 154, no. 2, pp. 131 – 142, 2003. 3.1.1

[33] W. Adam, S. Baffioni, F. Beaudette, D. Benedetti, C. Broutin, D. Chamont, C. Charlot, E. DiMarco, D. Futyan, S. Harper, D. Lelas, A. Martelli, P. Meridiani, M. Pioppi, I. Puljak, D. Sabes, R. Salerno, M. Sani, C. Seez, Y. Sirois, P. Vanlaer, and

D. Wardrope, "Electron Reconstruction in CMS." CMS AN-2009/164, January 2010. 3.1.2

[34] F. Beaudette, D. Benedetti, P. Janot, and M. Pioppi, "Electron Reconstruction within the Particle Flow Algorithm." CMS AN-2010/034, March 2010. 3.1.2

[35] CMS Collaboration, "Particle-Flow Event Reconstruction in CMS and Performance for Jets, Taus and E_T^{miss}." CMS Note PFT 2009/001, 2009. 3.1.2

[36] M. Pioppi, "Electron Pre-identification in the Particle Flow framework." CMS AN-2008/032, June 2008. 3.1.2

[37] M. Pioppi, "Iterative Tracking." CMS IN-200/005, November 2005. 3.1.2

[38] H.-J. Yang, B. P. Roe, and J. Zhu, "Studies of boosted decision trees for miniboone particle identification," *Nuclear Instruments and Methods in Physics Research Section A: Accelerators, Spectrometers, Detectors and Associated Equipment*, vol. 555, no. 1-2, pp. 370 – 385, 2005. 3.1.2

[39] T. Sjostrand, L. Lonnblad, and S. Mrenna, "PYTHIA 6.2: Physics and manual," 2001. 4.1

[40] S. Agostinelli *et al.*, "G4–a simulation toolkit," *Nuclear Instruments and Methods in Physics Research Section A: Accelerators, Spectrometers, Detectors and Associated Equipment*, vol. 506, no. 3, pp. 250 – 303, 2003. 4.1

[41] J. Allison *et al.*, "Geant4 developments and applications," *Nuclear Science, IEEE Transactions on*, vol. 53, pp. 270 –278, feb. 2006. 4.1

[42] A. P. Vartak, M. LeBourgeois, and V. Sharma, "Lepton Isolation in the CMS Tracker, ECAL and HCAL." CMS AN-2010/106, Jun 2010. 4.3.6

[43] R. Barlow, "Extended maximum likelihood," *Nuclear Instruments and Methods in Physics Research Section A: Accelerators, Spectrometers, Detectors and Associated Equipment*, vol. 297, no. 3, pp. 496 – 506, 1990. 4.6.1

[44] The CMS Collaboration, "Electromagnetic calorimeter calibration with 7 TeV data." PAS Public Analysis Note EGM-10-003, 2010. 5.3.1

[45] The CMS Collaboration, "Measurement of CMS Luminosity." PAS Public Analysis Note EWK-10-004, 2010. 5.4

[46] The CMS Collaboration, "J/Ψ prompt and non-prompt cross section in pp collisions at $\sqrt{s} = 7$ TeV." PAS Public Analysis Note BPH-10-002, July 2010. 5.5

List of Tables

List of Figures

List of acronyms

ALICE A Large Ion Collider Experiment

APD Avalanche Photo-Diode

ATLAS A Toroidal LHC ApparatuS experiment

BDT Boosted Decision Trees

CERN European Laboratory for Particle Physics

CMS Compact Muon Solenoid

COM Color Octet Mechanism

CSM Color Singlet Model

EB ECAL Barrel

ECAL electromagnetic calorimeter

EE ECAL Endcap

GSF Gaussian Sum Filter

HCAL hadron calorimeter

HLT Higher Level (software) Trigger

KF Kalman Filter

L1 Level 1 (hardware) trigger

LEP Large Electron Positron collider

LHC Large Hadron Collider

LHCb Large Hadron Collider beauty experiment

MC Monte Carlo

MIP Minimum Ionising Particle

NP New Physics

NRQCD Non-Relativistic QCD

PDG Particle Data Group

QCD Quantum Chromo-Dynamics

QCDDoubleEMEnriched QCD Double Electro Magnetic Enriched

pdf probability density function

$\mathrm{R_M}$ Molière Radius

SC Super Cluster

SM Standard Model

T&P Tag&Probe